

A STUDY OF OPTICAL OBSERVING TECHNIQUES FOR EXTRA-GALACTIC SUPERNOVA REMNANTS: CASE OF NGC 300

William C. Millar^{1,2}, Graeme L. White³ and Miroslav D. Filipović^{4,1}

¹*Centre for Astronomy, James Cook University, Townsville, Queensland 4811, Australia*

²*Grand Rapids Community College, 143 Bostwick N.E., Grand Rapids, MI, 49503, USA*
E-mail: wmillar@grcc.edu

³*Charles Sturt University, Locked Bag 588, Wagga Wagga, NSW 2678, Australia*

⁴*University of Western Sydney, Locked Bag 1797, Penrith South DC, NSW 1797, Australia*
E-mail: m.filipovic@uws.edu.au

(Received: October 30, 2011; Accepted: February 13, 2012)

SUMMARY: We present the results of a study of observational and identification techniques used for surveys and spectroscopy of candidate supernova remnants (SNRs) in the Sculptor Group galaxy NGC 300. The goal of this study was to investigate the reliability of using $[\text{S II}]:\text{H}\alpha \geq 0.4$ in optical SNR surveys and spectra as an identifying feature of extra-galactic SNRs (egSNRs) and also to investigate the effectiveness of the observing techniques (which are hampered by seeing conditions and telescope pointing errors) using this criterion in egSNR surveys and spectrographs. This study is based on original observations of these objects and archival data obtained from the Hubble Space Telescope which contained images of some of the candidate SNRs in NGC 300. We found that the reliability of spectral techniques may be questionable and very high-resolution images may be needed to confirm a valid identification of some egSNRs.

Key words. Supernova Remnants – Galaxies: Individual: NGC 300 – Galaxies: ISM – Astrometry – Telescopes – Techniques: Miscellaneous

1. INTRODUCTION

The Earth is located in the gas and dust filled disk of the Milky Way galaxy (here after, the Galaxy)

making the study of supernova remnants (SNRs) within the Galaxy difficult because the extinction and reddening effects of this interstellar medium (ISM) blocks or severely hampers our ability to see Galactic SNRs at wavelengths other than radio. For observations of SNRs in nearby galaxies this absorption by

the ISM within both the host galaxy and the Galaxy is greatly reduced – particularly for face-on (low inclination angle) spiral galaxies with high Galactic latitude (Matonick et al. 1997; Pannuti et al. 2000). Surveys of SNRs in the Local Group galaxies such as the Large and Small Magellanic Clouds (Filipović et al. 2005; Payne et al. 2008) and galaxies within some nearby clusters (mostly the Sculptor Group) have resulted in observations that are free from these biases. Over 450 SNRs have been found in nearby galaxies and listings are given by Matonick et al. (1997), Urošević et al. (2005), Filipović et al. (2008) and Pannuti et al. (2007).

An image of NGC 300 is shown in Fig. 1. Table 1 provides a brief list of the characteristics of NGC 300 following Millar et al (2011, here after, MWF11); a more complete list is provided by Kim et al. (2004). NGC 300 has a low inclination angle and a high Galactic latitude and observations of SNRs within NGC 300 suffer very low internal extinction (Butler et al. 2004) and foreground reddening¹. NGC 300 shows many giant H II regions which are evidence of many star formation episodes (Read et al. 2001). The similarities between NGC 300 and other nearby spiral galaxies (such as M 33 in the Local Group, and other members of the Sculptor Group, such as NGC 7793) lead us to conclude that NGC 300 is a typical, normal spiral galaxy (Blair et al. 1997, here after, BL97). Most authors have adopted distances of 2.0–2.1 Mpc for NGC 300 (BL97; Payne et al. 2004, here after P04; Table 1) hence, we have adopted this distance of 2.1 Mpc to be consistent with previous SNR surveys and spectral observations (BL97; P04). The corresponding linear scale is 10.2 pc arcsec⁻¹.

The resolving power (or seeing) of the two-meter class, ground-based telescopes usually used for SNR observations is generally from 0.5'' (Chil   up to 2'' (Siding Spring, Australia or Sutherland, South Africa). These seeing conditions do not allow the direct imaging of extra-galactic SNRs (here after, egSNRs) and therefore, spectral line intensity ratios are used for identification of these objects. The now common technique of using two narrow band optical interference filters, one centered on H   (λ 6564   ) and the second allowing passage of the [S II] ($\lambda\lambda$ 6717, 6731   ) doublet, to observe (or survey) bright nebulae in nearby galaxies was first described in a series of papers by Mathewson et al. (1972, 1973a,b,c). This technique depends on the strength of the [S II] lines in SNRs being about the same strength as the H   line, which is most likely due to shock fronts in the expanding SNR shell as it collides with a dense ISM. In H II regions (where there are few if any shock fronts) this condition would not exist. The total flux of the two [S II] lines should be at least an order of magnitude weaker than the H   line in H II regions as compared to SNRs (Math-

ewson et al. 1972). Because of the filter's bandwidth, the H   filter was not able to remove the [N II] ($\lambda\lambda$ 6548, 6583   ) doublet lines adjacent to the H   line. In some SNRs these lines (summed) can be as strong as the H   itself. Given this extra flux near the H   line, a candidate SNR was claimed if the emission region contained a (non-thermal) radio source and the H   + [N II] to [S II] ratio was less than two (Mathewson et al. 1972).

Dodorico et al. (1978) presents arguments based on observations of SNRs and H II regions within the Galaxy and with the Large Magellanic Cloud to show how SNRs can be identified within M 33 when [S II]:H   > 0.4. When [S II]:H   < 0.2 the nebula is considered a H II region (BL97). When [S II]:H   is between these two values the nature of the nebula may be unclear. Fesen et al. (1985) found that [O I] ($\lambda\lambda$ 6300, 6364   ), [O II] (λ 3727   ) and [O III] ($\lambda\lambda$ 4959, 5007   ) are often all simultaneously strong in SNRs and this can also be used to help differentiate SNRs from H II regions in cases where [S II]:H   is borderline.

The first observations of SNRs within NGC 300 using this technique were published by Dodorico et al. (1980). The candidates studied for this paper are the same candidates studied in MWF11 which were selected from those published by BL97 (optical candidates) and P04 (radio candidates). The positions of these SNRs and SNR candidates and the results of previous observations are given in Table 2 and are shown in Fig. 1. For Table 2, column 1 is the optical designation as given in BL97. Column 2 is the radio designation as given in P04. Columns 3 and 4 are the right ascension (RA) and declination (Dec) coordinates. Column 5 is the [S II]:H   as reported in (or derived from) BL97. Column 6 is the [S II]:H   as reported in MWF11 (including the measurement error discussed in MWF11). Column 7 is the spectral index (α) as reported in P04 and column 8 is the measured diameter as reported in MWF11.

In MWF11, these candidates were studied with long-slit spectral observations and the accepted criteria ([S II]:H   \geq 0.4 and the presence of [O I]) were used giving a result of 22 objects as SNRs, with the remaining left as unknown (no signal) or unclear. For some of those objects which were unclear, the error in the [S II]:H   measurement allows overlap with the [S II]:H   \geq 0.4 threshold. The radio sources which do not reach the threshold value to be labeled as optical SNRs may be optically obscured by the emissions from neighboring H II regions (P04). This possibility is further supported by our investigation of the radio observations' astrometry here (section 3.1). There are other well established causes for the poor overlap of observed radio and optical SNR emissions (Duric. 2000a,b).

In this paper we investigate the reliability of using [S II]:H   \geq 0.4 as a defining criterion for the

¹ $E(B - V) = 0.013$ mag (Bland-Hawthorn et al. 2005).

detection and identification of egSNRs, and the effectiveness of the observing techniques used for egSNR surveys and spectrographs. We present a study of comparisons of the observations of these SNR candidates between BL97, P04, MWF11 and images containing the candidates found in the archives of the Hubble Space Telescope (HST). For reasons given below, this study included an analysis of the astrometry of the original CCD images from BL97, a discussion of the astrometry of the radio observations from P04, and an analysis of the pointing errors inherent in the two-meter class telescopes generally used for egSNR observations. Even with good seeing conditions, this telescope size class may be too small to ensure the reliability of using the [S II]:H α ratio to identify egSNRs with complete confidence.

We found five sources which were comparable between the observation sets – four radio sources and one optical source. We found an apparent systematic error in the radio observation astrometry. Unfortunately, with only four radio sources to work with in the current HST data, testing this possible error any further requires more high-resolution (HST) optical images. Only one source was in both the BL97 and HST observations. However this one source demonstrated a need for further investigation into the reliability of using the [S II]:H α line ratio for the identification of egSNRs in optical surveys and spectral observations.

2. NGC 300 SNRs IN THE HST ARCHIVAL DATA

Table 3 shows the file names associated with the central wavelengths sorted by wavelength along with the original proposal identification and any publications based on the data. In this table, column 1 is the central wavelength of the HST filter, column 2 is the file name (all with .FITS extension) containing the image, column 3 is a list of publications associated with the observation. The references are included to provide the original objectives of the observations of NGC 300 at these wavelengths and other publications which have used these observations (all taken from the MAST² web site).

Table 4 shows the bandwidths for each of the HST filters used for these images. These data were taken from the images' FITS file header³. Column 1 is the filter's central wavelength and column 2 is the filter bandwidth. This table also shows emission wavelengths with the associated ions or atoms that are found within the bandwidth of the filters (column 3). These ions or atoms are known to be within (Galactic) SNRs (Fesen et al. 1996).

A computer program was written to read the HST FITS file headers and based on each file's FITS world coordinate system (WCS) the following objects (from Table 2) were found in one or more of the images files: J005438–374144, J005440–374049, J005445–373847, J005450–374030, J005450–373822, J005450–374022, J005451–373826, J005451–373939, J005500–374037, J005501–373829, J005503–374246, J005503–374320, N300-S8, N300-S9, N300-S10, N300-S13, N300-S14, N300-S15, N300-S16, N300-S18.

Table 5 lists the filter central wavelengths and bandwidths containing spectral emissions which are diagnostic to the identification of SNRs (see discussion in section 1). This table's columns are the same as those in Table 4. The emissions of most interest are: H α (λ 6565 Å), [S II] (λ 6717 Å, λ 6732 Å), [O I] (λ 6300 Å), and [O III] (λ 5007 Å). Only the files possibly containing these wavelengths were examined any further. As can be seen from Table 3, only one image file group contains data with H α (u671370#r_drz, where # is one of the digits, 5 to 9). There were no files containing the [S II] doublet wavelengths. The images centered on λ = 5741 Å and λ = 6001 Å contain wavelengths of interest but none of these images contain objects from Table 2. Thus, only the H α images were of use for this study. Only 5 of the 51 objects were found within the H α images. All of the H α images have the same field of view. The final results of the search are shown in Table 6. The columns from this table are the same as those for Table 2.

The HST H α images are centered on (00^h54^m54^s.54, –37°40'35".9). They are 400 second exposures taken in May of 2001 with the Wide-Field Planetary Camera 2 (WFPC2) instrument using its (default) PC1 aperture. The filter used in these images (F656N) was centered on λ = 6563.76 Å with a RMS bandwidth of $\Delta\lambda$ = 53.77 Å. The bandpass characteristics of this filter are shown in Fig. 2. The data were originally collected as part of the HST proposal 8591 by, Douglas Richstone (Richstone. 2000). The file u6713709r_drz.fits appeared to provide the cleanest image for analysis of the SNR candidates' environment.

Figure 3 shows the image contained in this file in negative gray-scale. The five SNR candidates (Table 6) in the field of view are labeled and positioned by DS9 pandas. For comparison, Fig. 4 shows an image with the same position, size and rotation using DSS2-Red data from SkyView⁴. There is a slight difference in plate scale between the two images. The green line in Fig. 4 is the outline of the HST image's (Fig. 3) first quadrant, which contains the high-resolution CCD chip and the center of NGC 300. A bright star in the second quadrant which appears in the DSS2-Red image does not appear in the HST im-

²<http://archive.stsci.edu/>

³They are also available on the HST WFPC2 instrument website. <http://www.stsci.edu/hst/wfpc2/documents/IHB.17.html>

⁴<http://skyview.gsfc.nasa.gov/>

age (the DSS2-Red survey includes $H\alpha$ wavelengths). There are some differences in the apparent distribution of gas in the DSS2-Red image compared to the HST image, probably due to the wider pass band of the DSS2-Red image. There is a triangular shaped optical artifact located to the north of the very bright star near the bottom of the DSS2-Red image. The four radio SNR candidates from P04 were not optically confirmed, the optical SNR candidate from BL97 was confirmed (MWF11, Table 2).

3. ANALYSIS OF THE RADIO SOURCES

When the HST image was displayed in false color⁵ to show emission intensity (Figures 5 through 8), a number of small sized, high intensity objects appeared in the image. Most likely these are stars but that is difficult to determine from the available data. Here after these objects are referred to simply as “hot spots.”

Multi-frequency observations of egSNRs are limited by current technologies to radio, optical and X-ray emissions. None of the four radio sources found in this HST image are known to have emissions in other wavelengths. NS16 is observed only in optical.

3.1 Radio Observations Astrometry

The majority of the SNRs found in the Galaxy and the Magellanic Clouds are 50 pc or less in diameter (Strom, 1996). If the same is assumed for NGC 300, then the SNRs in NGC 300 should be less than $5''$ in diameter (at the assumed distance). The radio observations published in P04 used a circular beam width of $6''$. Thus the typical SNR would not fill the beam of the radio telescope. This may have led to systematic astrometric errors.

In Figures 3 through 8 the images (particularly the HST $H\alpha$ images) appear to show that there is such a systematic error in the astrometry of the radio candidates. The candidates show a consistent displacement to the southwest from the neighboring H II region. To account for radio emissions typical of a SNR without corresponding optical emissions (particularly when the candidate is ~ 50 pc in diameter) the radio source should be located within or adjacent to the H cloud region so the candidate SNR’s optical emissions could be masked. Though this is not the only possible explanation for such candidate SNR radio/optical observations (Duric, 2000a,b; Pannuti et al. 2000), it is likely (P04). No ground-based telescope of less than four meters should be able to separate this candidate from the H II region.

Radio observations with a higher resolving power or very high-resolution optical observations

(HST) of the other radio sources are needed to resolve this possible apparent error.

3.2 SNR Candidate J005450–374030

This radio SNR candidate has a spectral index of -0.5 ± 0.2 . It has a $[S II]:H\alpha$ of 0.32 ± 0.12 (MWF11, Table 2). Because the threshold value of the $[S II]:H\alpha$ is 0.4 this candidate could not be classified as an optical SNR (MWF11). Note however that the threshold value is within the error of the line ratio measurement. Figure 5 shows the detail in the HST image at the location of this radio source. The candidate is located very near the edge of a H II region (H II C29, Soffner et al. 1996, $8.33''$, 85 pc away from center) showing no special structural properties.

A single image in $H\alpha$ does not allow us to determine the nature of the emissions from the region. An HST $[S II]$ image would be very helpful. If there is a systematic error in the astrometry of the radio source, it is possible that the radio source is actually inside the H II region and the H II region would then interfere with the optical line ratio measurement. There are many known SNRs without optical emission so some of the NGC 300 SNRs would be expected to be in that group.

3.3 SNR Candidate J005450–374022

Figure 6 shows detail in the HST $H\alpha$ emissions surrounding the radio source J005450–374022 which was classified as being either a SNR or a H II region in P04. The radio source is located on the edge of a large bubble in the H II region (76C, Deharveng et al. 1988, $2.36''$, 24 pc away from center). The small magenta ($1''$) circle pointed out by the red arrow shows the position of the candidate. The larger magenta ellipse (at the edge of which the radio candidate is located) outlines one possible border to the large bubble. A smaller region within the ellipse which can be seen at the green emission level may also be a SNR shock front within this H II region. Without proper $[S II]$ data these remain simply possibilities of shock fronts.

The magenta ellipse is $2.54'' \times 2.38''$ or 25.9×24.8 pc with its semi-major axis aligned in declination. This is approximately the size of an SNR of about 10 000 to 20 000 years in age (Cioffi, 1990). SNRs of this age are typically in the radiative, pressure-driven snowplow (PDS) stage which likely presents a bubble shaped appearance such as the one seen in this image. The $[S II]:H\alpha$ for this candidate is 0.38 ± 0.31 (MWF11, Table 2). While the ratio is just below the critical value of 0.40, the large noise error in this measurement combined with the apparent structure next to the radio candidate raises serious concern about denying its classification as an optical

⁵Using the Smithsonian Astrophysical Observatory’s DS9 software package <http://hea-www.harvard.edu/RD/ds9/>.

SNR. This evidence is only available because of this high resolution image from the HST.

Also shown in Fig. 6 is a black line corresponding to the diameter measurement of this candidate (130 pc) as published in MWF11. This allows comparison of the poorer seeing conditions during those observations with the resolution of the HST image. This 130 pc ($\sim 12.7''$) line is drawn centered on the published position of the radio source. Given this diameter comparison, the [S II]:H α may be that of the H II region with a large error caused by seeing conditions. No firm conclusion about the optical emissions of this radio source can be drawn from these data with the seeing conditions degrading the line ratio technique by increasing the measurement error.

3.4 SNR Candidate J005451–373939

Figure 7 shows the location of J005451–373939, next to an H II region (#20, Bresolin et al. 2009, $3.80''$, 39 pc away from center). This H II region has a bright emission source off to one side at the same location as the radio source. It is not likely this “hot spot” could be the SNR but it could be the known Wolf-Reyet (WR) star from (#18, Schild et al. 2003). There is also a known star association in this region (AS 57, Pietrzyński et al. 2001). Emissions from these stars (the association or the WR) can not be separated from the SNR candidate in the spectrographic slit and the WR star may also contribute to the radio emissions (we note the discussion of excessive radio emissions and the spectral index of Galactic WR stars in Montes et al. (2009)).

This radio source could be a SNR within the H II region or it could be a coincidence with a combination of stars. Observations with the HST’s WFPC2 instrument using the F673N filter to indicate the presence of any [S II] emission could be very helpful here. The spectroscopic measurements from MWF11 do not support this object as an SNR.

3.5 SNR Candidate J005500–374037

Figure 8 shows the location of the SNR candidate J005500–374037. The radio source is outside of any notable H α emission. There is a large inset into the H II region (H II E18, Soffner et al. 1996, $4.45''$, 45 pc away) on the side nearest the radio source. However, if this inset were due to a supernova event the SNR would definitely be in the PDS stage and both radio and optical emissions should be coming from the shock front, not from the center of, or outside of the expanding shock. There are at least four known H II regions, a planetary nebula and a star association in the vicinity of this radio source but they

are far enough from the source that they should be separable in the spectrometer slit – given the correct source astrometry and telescope pointing. There is a possibility that this radio source is a background object (e.g. a quasar) which happens to lie very near a H II region within NGC 300 although this source was classified as an SNR as opposed to SNR/H II region in P04. As has been mentioned previously, this could also be a SNR without optical emissions.

If the apparent systemic radio astrometry error is real, it may be an SNR with its optical emissions masked by the H II region emissions. The emissions from the SNR and the H II region would be impossible to distinguish with a two-meter class telescope.

4. ANALYSIS OF THE OPTICAL CANDIDATE

The N300-S16 [S II]:H α ratio was not measured from spectra in BL97 but Table 3A of that paper shows N300-S16 with a [S II]:H α of 0.70, based on the BL97 survey CCD images. BL97 also reports a (H α) diameter of 52 pc. From MWF11, N300-S16 has an observed [S II]:H α of 0.94 ± 0.06 and a measured diameter of 57 pc. This large measured ratio is based on fairly low flux levels: H α = 2.2 and [S II] = $2.1(10^{-15} \text{ erg cm}^{-2} \text{ s}^{-1})$.⁶ Hoopes et al. (1996) demonstrated that a [S II]:H α of up to 0.5 can be created by the diffuse ionized gas (DIG) of NGC 300. Because this candidate is not near any known H II region this “background ratio” could be subtracted from the MWF11 ratio and the result still exceeds the 0.4 critical [S II]:H α ratio for indication of an SNR. However, the critical value is then within the small noise error.

Figure 9 shows the BL97 images (set G) of N300-S16 zoomed and cropped. On the left is the H α filter image and on the right is the [S II] filter image. In both images only a faint increase from the background is seen at N300-S16’s given position. The inner panda circle is centered on the N300-S16 coordinates with an apparent $8''$ (81.6 pc) diameter – somewhat larger than the measured diameter. The outer panda circle is twice as big.

Figure 10 zooms in to the HST H α image at N300-S16. In this figure there is no evidence of any structure in the H α emissions. It is possible that the [S II]:H α test for SNR character has failed. No satisfactory explanation of the apparent contradiction between the two observations has been found.

⁶The BL97 candidates’ spectral flux density was consistently weaker by an order of magnitude compared to the P04 candidates. (See MWF11.)

5. THE ASTROMETRY OF BL97

There is contradictory evidence for the existence of a SNR at the location labeled as N300-S16. BL97 and MWF11 have high $[\text{S II}]:\text{H}\alpha$ values but the HST $\text{H}\alpha$ image shows no indication of any structure in the vicinity. In an attempt to find a resolution we checked the astrometry of the BL97 CCD images. The CDD images used for the BL97 optical survey were provided by, William Blair. These images were sets and each set was labeled with the letters ‘C’ through ‘J.’ Each lettered image set contained a continuum image, a $\text{H}\alpha$ filter image and a $[\text{S II}]$ filter image with the same center, plate scale and rotation (see BL97). The files did not include the ‘I’ image (which was used in BL97) but did include a ‘K’ image which was not used in BL97. The ‘I’ image contained SNR candidates N300-S12 and N300-S17. The ‘C’ and ‘K’ images contained no SNR candidates and thus were not considered in this analysis.

The images are in the flexible image transport system (FITS) format, 800 pixels on a side, with a field of view of approximately 0.087° . The central coordinates of each image are given in Table 2 of BL97. The image files did not have a FITS WCS and the x -axis needed to be inverted to obtain the correct orientation (north up and east to the left). A WCS was thus created for each of the FITS files.

5.1 Finding Known Objects Within the Images

A list of 2MASS point sources from the online catalog was created from a search for all sources within a radius of one arc-degree of the center of NGC 300. The program used a dynamic array of a record structure to store the coordinates of each 2MASS point source along with a “distance” data field, which is discussed below. NASA’s SkyView was used to create DSS and DSS2-Red FITS file images which appeared equivalent to the BL97 images. The SkyView 2MASS images were used as a visual aid in associating bright, easy to locate 2MASS point sources with optical counterparts in each BL97 image. To reduce errors in calculating the image scale the chosen sources were always closer to (but not at) the edge of the image.

The BL97 (x, y) coordinates and 2MASS (α, δ) coordinates of each of the three 2MASS sources from each image were entered into a computer program. The estimated coordinates were compared to the list of catalog coordinates. The comparison created a distance measurement between the estimated and the catalog coordinates which was stored in the “distance” data field of each point source data record structure. The source list was then sorted on the distance field and the source with the smallest distance was put at the top of the sorted list. The catalog coordinates at the top of the list were the coordinates

actually used for calculating the BL97 image center, plate scale and rotation.

5.2 Program Results and Astrometry of the SNRs

Table 7 shows the program results for the calculation of the image centers. Column 1 is the image identification letter. Column 2 is the image center as given in BL97’s Table 2. Column 3 is the calculated center from the program and column 4 is the distance (or offset) between them, in arcseconds.

After studying the continuum, $\text{H}\alpha$ filter and $[\text{S II}]$ filter images for each lettered image set, any difference in the center coordinates between the image filter types appeared to be negligible. Because the filters used to make the $\text{H}\alpha$ and $[\text{S II}]$ images were narrow band, it was impossible to locate 2MASS point sources within those images. Thus, center coordinates and plate scale values were calculated only for the continuous images and then applied to all image filter types for the image field (lettered set). Based on the calculated WCS for each image, Table 8 shows the reported equatorial and calculated pixel coordinates for each of the BL97 SNR candidates.

N300-S16 is the only BL97 SNR candidate to appear in an HST image. Figure 11 shows the BL97 $\text{H}\alpha$ filter and $[\text{S II}]$ filter images of N300-S1 (image set D). The pandas mark the coordinates given for N300-S1 in BL97 as calibrated by 2MASS point sources. The BL97 astrometry is good – certainly within the seeing conditions reported in BL97 ($\sim 1''$). Figure 12 shows a comparison of the reported position (BL97, on left) of N300-S16 with the apparent center of the assumed image of the candidate (HST, on right). The offset in these positions ($0.7''$) is again within the reported seeing conditions. The logical next step would be to calibrate the HST images to 2MASS and study the HST $\text{H}\alpha$ image of N300-S16 in comparison to the BL97 images.

6. HST IMAGE ASTROMETRY

The HST FITS file headers indicated that the HST Guide Star Catalog (GSC) version 1.x was used for the image astrometry. According to the Astrometry Department of the United States Naval Observatory⁷ the accuracy of this catalog is approximately 500 mas. The biggest problem with the GSC is that it does not provide for the proper motion of the stars.

The attempt to calibrate the HST images to the 2MASS catalog using the procedure and software from the BL97 analysis proved to be impractical because of the high-resolution of the HST images. The difference in resolution between the SkyView 2MASS

⁷http://ad.usno.navy.mil/star/star_cats_rec.shtml

images and HST images made it impossible to correctly identify 2MASS point sources in the HST images with reasonable confidence. Therefore we used an alternative method to check the astrometry.

6.1 Alternate Analysis

An analysis of the HST and DSS2-Red files' WCS accuracy against the BL97 2MASS-calibrated images was made by comparing the position of a bright star which could be identified in all image sets. The first comparison, between BL97 and the HST images, is shown in Fig. 13. On the left is the BL97 G H α image containing N300-S16 and on the right is the HST H α image containing N300-S16. The position of the selected star within these images is listed in Table 9. In this table column 1 is the image used for the observation (BL97, HST, DSS2-Red), columns 2 and 4 are the J2000 RA and Dec coordinates of the center of the image of the star as found using DS9. Table 9 columns 3 and 5 are the difference between the positions (with BL97 as the reference) in arcseconds. Column 6 is then the difference in position (offset) between the two images, measured in arcseconds. Between the BL97 and HST images there is an offset of $0.15''$.

The second comparison was made between BL97 and the DSS2-Red images used for the finding maps for the observations in MWF11 and is shown in Fig. 14. Between the BL97 and DSS2-Red images there was an offset of $0.13''$. Mickaelian (2004) measured the astrometry of the DSS2-Red images based on AGN positions and found an accuracy of $0.33''$. These comparisons demonstrate that any error in the astrometry of the images used in BL97 was within the reported seeing conditions.

6.2 Estimating Positional Error

Because of the difficulty in recalibrating the HST image WCS the alternative procedure of convolving the position errors was used. In section 5.2 it was found that the position error in the BL97 images was $\sim 1''$ (mainly due to seeing). This was convolved with the approximate positional error of the HST images from Table 9 to find a positioning error of the BL97 SNRs on the HST images: The result is $1.0''$ – essentially the seeing conditions of BL97. The same was done with the radio SNRs from P04. According to Table 2 of P04 these candidates were observed with a circular beam width of $6''$. Convolution 10% of that gives a 1σ positioning error for the candidates as $0.62''$ or $0.6''$.

These values were used as the 1σ positioning error for finding the SNR candidates within the HST images. We see that positioning (astrometry) errors are due mainly to seeing conditions and telescope pointing.

7. SEEING AND TELESCOPE POINTING

Some of the candidates from BL97 which were observed in MWF11 returned no signal. In an attempt to determine the cause, the telescope pointing accuracy was analyzed by superimposing the slit camera images on top of the observation finding maps. Figures 15 and 16 show examples of the results. Figure 15 shows a very good alignment with N300-S2. In Fig. 16 there is a confusion of sources surrounding N300-S11. Both N300-S11 and J005442–374313 were clearly within the slit and the seeing conditions were undoubtedly allowing J005443–374311 to also flow through. Exactly what was being measured here is uncertain but it was labeled as N300-S11 (MWF11) because it was the principle candidate for that observation. This observation also included emission from the neighboring H II region.

For N300-S11, BL97 reports $[S II]:H\alpha = 0.66$ (based on CCD images, not spectra) and MWF11 reports $[S II]:H\alpha = 0.30 \pm 0.12$. Because of source confusion, neither of these measurements can be trusted. BL97 claimed seeing of $1''$, but these sources would be confused in any spectrometer's slit. Due to seeing conditions creating telescope positioning error and the astrometry error in the radio observations it is not possible to determine if J005442–374313 and N300-S11 are actually the same object. Measurements of the diameter of N300-S11 (BL97, MWF11) are greater than 100 pc. This large diameter may be caused by source confusion with the H II region or it may be a multiple supernovae site. Unfortunately multiple SNR sites are usually linked to OB associations and there are no known OB associations in this region. The only way to resolve this problem is with a higher-resolution telescope with no seeing problems – the HST. Unfortunately no archival HST file contained an image of these candidates.

Figure 17 shows the slit camera image on the finding map of N300-S16 used for the observations for MWF11. For this candidate the telescope pointing was erroneous (by $1''$ to $2''$ or 10 to 20 pc) and yet a $[S II]:H\alpha = 0.94 \pm 0.06$ was measured. The cause of the poor alignment is difficult to determine – equipment or seeing conditions. It is most likely due to seeing conditions which were on the order of two to three arcseconds for most nights of the observing run. The seeing conditions may have allowed most of the flux from N300-S16 through the slit but it is then difficult to account for the higher ratio compared to the BL97 results (0.70).

However, we still have the real problem with this observation – the HST image containing N300-S16 shows no evidence of the candidate's existence (Fig. 10).

8. ANALYSIS OF THE BL97 IMAGES

BL97 obtained long slit spectra for $\sim \frac{2}{3}$ of the candidates found in the optical filter survey for that paper. With 100% confirmation ($[\text{S II}]:\text{H}\alpha > 0.4$) of this $\frac{2}{3}$ sample, there was confidence in all 28 candidates being confirmed as SNRs (Long. 1996). N300-S16 was not a member of that $\frac{2}{3}$ subset.

8.1 Candidate Image Profiles

Optical emissions are expected to be greatest during the PDS stage (Cioffi. 1990). This stage is typically 50 pc at maximum diameter. At the distance to NGC 300 50 pc is equivalent to $4.9''$. The images for BL97 are 800×800 pixels at 5.3 arcminutes square (BL97; Long. 1996) and the pixel size is then $0.4''$. At the distance to NGC 300 this is about 4 pc. The maximum theoretical size of a PDS stage SNR on a BL97 image would be about 12 pixels in diameter or an area of about 110 pixels squared.

The $\text{H}\alpha$ and $[\text{S II}]$ images used for BL97 were analyzed for candidate image profiles with the intention of investigating the actual number of CCD pixels used to determine the $[\text{S II}]:\text{H}\alpha$ ratio of the candidate SNRs. Using the “Co-Add” command of SBIG’s *CCDOps* program⁸ the image of each SNR candidate was stacked to form a composite image. This was done with both the $\text{H}\alpha$ and $[\text{S II}]$ images. The x and y -axis profiles of these composite images are shown in Figures 18 and 19.

Figure 18 shows two renditions of the stacked $\text{H}\alpha$ candidate images. These two renditions differ by the display intensity scale and the number of plotted contour lines. The images were stacked so all SNR candidates were located (the pixel corresponding to their equatorial coordinates) at the same resultant pixel. The rendition on the right has the crosshairs and profiles centered on the emissions peak which happens to be the same as the coordinate pixel. As an example of the data, Table 10 shows a 9×9 grid of the CCD pixel values from Fig. 18. Figure 20 shows a surface plot of these values which clearly shows a high signal level against the background. Figure 21 shows a line plot the values along the x -axis (E-W) at y -axis (N-S) row number 165. The full-width half maximum is about 10×12 pixels ($\sim 41 \times 49$ pc) which is about the same as the expected 12 pixel diameter area and the most expected diameter for candidates at this stage of their evolution.

In Fig. 19 the $[\text{S II}]$ frames were stacked but did not include the H and J images as these were too noisy for this procedure. Various techniques were used to remove the noise⁹. The problem was that

the $[\text{S II}]$ signal on these images was too close to the noise floor. The H and J images contained candidates: N300-S2, S3, S4, S7 (H image); S20, S26, S27 (J image). Figure 19 shows two renditions of the stacked $[\text{S II}]$ images. On the left the crosshairs (and the profiles) are centered on the coordinate pixel (508, 164). On the right, the crosshairs (and profiles) are centered on the pixel with maximum value (509, 162). This difference in pixel position corresponds to about 4 (RA) and 8 pc (Dec) in physical distance, respectively. The SNR positions were determined from the $\text{H}\alpha$ images based on H II regions but this also implies that the maximum $\text{H}\alpha$ and the maximum $[\text{S II}]$ emissions are on the opposite side of the SNR. The surface plot of the $[\text{S II}]$ emissions shown in Fig. 22 shows multiple peaks distributed around the centers of the SNR candidates. The FWHM (centered on the greatest peak) is about 9×9 pixels ($\sim 37 \times 37$ pc).

The estimated FWHM of $\text{H}\alpha$ and $[\text{S II}]$ profiles were convolved with the FWHM of a small star from the $[\text{S II}]$ J image. The profile of the star is shown in Fig. 24. When the FWHM of the stacked $[\text{S II}]$ image profile (Fig. 23) was convolved with the small star image profile (Fig. 24) the resulting apparent size of the stacked $[\text{S II}]$ regions was,

$$\sqrt{(28 \text{ pc})^2 - (15 \text{ pc})^2} = 23 \text{ pc} = 6 \text{ pixels} \quad (1)$$

This was taken as the average SNR candidate diameter, so the extant image area of the $[\text{S II}]$ emissions was approximately 28 pixels squared. Because the images could not be flux calibrated, the number of pixels actually contributing to the $[\text{S II}]:\text{H}\alpha$ could not be estimated with reasonable confidence. The theoretically expected maximum number of pixel was about 110. With only 28 pixels (in a stacked image of all sources) contributing to the flux measurement of spectra, flux measurements of BL97 may well have large errors. Weak signals may lead to large flux measurement error (as an overestimate) an effect noted in other egSNR observations by Blair et al. (1981).

8.2 Images of N300-S16

Figure 11 shows the BL97 $[\text{S II}]$ and $\text{H}\alpha$ images zoomed in on N300-S16. As measured in MWF11 the $\text{H}\alpha$ and $[\text{S II}]$ flux levels for N300-S16 were about $2 \times 10^{-15} \text{ erg cm}^{-2} \text{ s}^{-1}$ which was only about 100 CCD pixel counts above the background. The spectrum shows a high-level background along the slit. Figure 17 shows the slit was at least an arcsecond away from the reported coordinates of the candidate. The spectrum from MWF11 of N300-S16 is shown in Fig. 26.

In the HST $\text{H}\alpha$ image of N300-S16 (Fig. 10) there was little if any evidence of a disturbance in the H gas in the region of the location of N300-S16.

⁸Available from Santa Barbara Instruments Group, <http://www.sbig.com/sbwhtmls/ccdopsv5.html>

⁹*CCDOps* has some noise treatment routines such as, “Kill Hot Pixels,” “Kill Cold Pixels,” “Smooth Pixels.”

While the equivalent images of the radio SNR candidates (see Figures 5, 6, 7 and 8) show strong evidence of such, even though the measured $[\text{S II}]:\text{H}\alpha$ ratio does not confirm them as optical SNRs. There is also no known X-ray emission associated with N300-S16.

Figure 27 shows a 3-D plot of the BL97 CCD $\text{H}\alpha$ (top) and $[\text{S II}]$ (middle) image pixel counts of N300-S16. The pixels plotted (a 27×27 array centered on the candidate's coordinates) are shown by the green box in the image tile on the left. The plot is shown on the right. In both cases the emission is only slightly above the background but clearly discernible. The size of the candidate (50 pc) implies it to be at the end of its PDS stage. The 3-D plot on the bottom of the figure is a plot of the result of dividing the $[\text{S II}]$ pixel value by the $\text{H}\alpha$ pixel value. The apparent SNR disappears in the high-level DIG noise.

There are spectral line characteristics other than $[\text{S II}]:\text{H}\alpha$ to support SNR candidacy (e.g. the presence of $[\text{O I}]$ in the spectrum) and there is a selection effect biased toward finding SNRs away from H regions in optical surveys (P04). Type Ia SN which are away from any H region are then located in less dense ISM. As a result, there is a lower abundance of shocked material to produce the $[\text{S II}]$ (and other metallic) spectral lines in the SNR remnant. Such SNR spectra may be dominated by the Balmer lines (e.g. SN1006, Tycho's and Kelper's SN) and are generally missed by optical surveys (Pannuti et al. 2000). A check of the data from MWF11 shows no Balmer dominance in the spectrum of N300-S16, particularly with a $[\text{S II}]:\text{H}\alpha$ of 0.6 and a high level of $[\text{O I}]$ usually associated with shocked ISM. High-resolution imaging should be used to confirm the existence of this SNR. This imaging could be done with space-based telescopes (HST) or with four-meter class telescopes. Better results may be obtained with ground-based telescopes using adaptive optics.

9. CONCLUSION

A careful investigation of the data collected with the telescopes and instruments typically used for the discovery and confirmation of extra galactic supernova remnants reveals that the reliability of these techniques may be questionable. A strict flux density measurement error analysis shows that large errors in the $[\text{S II}]:\text{H}\alpha$ ratio occur when the ratio is based on low flux density levels (MWF11). Seeing conditions lead to blurring of telescope positioning and thus pointing errors which may impinge in the reliability of the flux measurements and on the confidence of exactly what object is being measured (Fig 17).

The seeing conditions also introduce error into the astrometry of the sources which is generally as large as the telescope pointing error. If these errors add in the same direction there is a possibility that the spectrograph slit is completely off the candidate. In cases where the target galaxy has high level emission from its diffuse ionized gas (such as NGC 300), the spectroscopic signal may not be sufficient to confirm the presence of a supernova remnant. High resolution optical images from space-based telescopes or from ground-based telescopes using adaptive optics may be necessary for confirming the existence of these extra-galactic supernova remnants.

Acknowledgements – We gratefully acknowledge the generosity of Professor William Blair who provided us with the original CCD image files from the BL97 survey observations. We also thank the Hubble Space Telescope archival team for their work in maintaining the archives thus making the telescope's original data available to all.

REFERENCES

- Andersen, D.R., Walcher, C.J., Böker, T., Ho, L.C., van der Marel, R.P., Rix, H., Shields, J.C.: 2008, *Astrophys. J.*, **688**, 990.
- Barth, A.J., Strigari, L.E., Bentz, M.C., Greene, J.E., Ho, L.C.: 2009, *Astrophys. J.*, **690**, 1031.
- Beifiori, A., Sarzi, M., Corsini, E.M., Dalla Bontà, E., Pizzella, A., Coccato, L., Bertola, F.: 2009, *Astrophys. J.*, **692**, 856.
- Berger, E., Soderberg, A.M., Chevalier, R.A., Fransson, C., Foley, R.J., Leonard, D.C., Debes, J.H., Diamond-Stanic, A.M., Dupree, A.K., Ivans, I.I., Simmerer, J., Thompson, I.B., Tremonti, C.A.: 2009, *Astrophys. J.*, **699**, 1850.
- Blair, W.P., Long, K.S.: 1997, *Astrophys. J. Suppl. Ser.*, **108**, 261.
- Blair, W.P., Kirshner, R.P., Chevalier, R.A.: 1981, *Astrophys. J.*, **247**, 879.
- Bland-Hawthorn, J., Vlajić, M., Freeman, K.C., Draine, B.T.: 2005, *Astrophys. J.*, **629**, 239.
- Böker, T., Lisenfeld, U., Schinnerer, E.: 2003a, *Astron. Astrophys.*, **406**, 87.
- Böker, T., Stanek, R., van der Marel, R.P.: 2003b, *Astron. J.*, **125**, 1073.
- Böker, T., Laine, S., van der Marel, R.P., Sarzi, M., Rix, H., Ho, L.C., Shields, J.C.: 2002, *Astron. J.*, **123**, 1389.
- Böker, T., Sarzi, M., McLaughlin, D.E., van der Marel, R.P., Rix, H., Ho, L.C., Shields, J.C.: 2004, *Astron. J.*, **127**, 105.
- Bond, H.E., Bedin, L.R., Bonanos, A.Z., Humphreys, R.M., Monard, L.A.G.B., Prieto, J.L., Walter, F.M.: 2009, *Astrophys. J. Lett.*, **695**, 154.
- Bresolin, F., Pietrzyński, G., Gieren, W., Kudritzki, R.: 2005, *Astrophys. J.*, **634**, 1020.
- Bresolin, F., Gieren, W., Kudritzki, R.P., Pietrzyński, G., Urbaneja, M.A., Carraro, G.: 2009, *Astrophys. J.*, **700**, 309.
- Butler, D.J., Martínez-Delgado, D., Brandner, W.: 2004, *Astron. J.*, **127**, 1472.
- Cao, C., Wu, H.: 2007, *Astron. J.*, **133**, 1710.
- Cioffi, D.: 1990, in Brinkmann, W., Fabian, A., Giovannelli, F., eds, *Physical Processes in Hot Cosmic Plasmas*, Kluwer Academic Publishers, Boston, 1.
- Dai, H., Wang, T.: 2008, *Chinese J. Astron. Astrophys.*, **8**, 245.
- Dalcanton, J.J., Williams, B.F., Seth, A.C., Dolphin, A., Holtzman, J., Rosema, K., Skillman, E.D., Cole, A., Girardi, L., Gogarten, S.M., Karachentsev, I.D., Olsen, K., Weisz, D., Christensen, C., Freeman, K., Gilbert, K., Gallart, C., Harris, J., Hodge, P., de Jong, R.S., Karachentseva, V., Mateo, M., Stetson, P.B., Tavarez, M., Zaritsky, D., Governato, F., Quinn, T.: 2009, *Astrophys. J. Suppl. Ser.*, **183**, 67.
- de Grijs, R., Wilkinson, M.I., Tadhunter, C.N.: 2005, *Mon. Not. R. Astron. Soc.*, **361**, 311.
- de Mello, D.F., Smith, L.J., Sabbi, E., Gallagher, J.S., Mountain, M., Harbeck, D.R.: 2008, *Astron. J.*, **135**, 548.
- de Vaucouleurs, G., de Vaucouleurs, A., Corwin, H.G. Jr., Buta, R.J., Paturel, G., Fouque, P.: 1991, *Third Reference Catalogue of Bright Galaxies*, Springer, New York.
- Deharveng, L., Caplan, J., Lequeux, J., Azzopardi, M., Breysacher, J., Tarenghi, M., Westerlund, B.: 1988, *Astron. Astrophys. Suppl. Ser.*, **73**, 407.
- Dodorico, S., Benvenuti, P., Sabbadin, F.: 1978, *Astron. Astrophys.*, **63**, 63.
- Dodorico, S., Dopita, M.A., Benvenuti, P.: 1980, *Astron. Astrophys. Suppl. Ser.*, **40**, 67.
- Duric, N.: 2000a, in Berkhuijsen, E.M., Beck, R., Walterbos, R.A.M., eds, *Proceedings 232. WE-Heraeus Seminar*, 127.
- Duric, N.: 2000b, in Berkhuijsen, E.M., Beck, R., Walterbos, R.A.M., eds, *Proceedings 232. WE-Heraeus Seminar*, 179.
- Fesen, R.A., Hurford, A.P.: 1996, *Astrophys. J. Suppl. Ser.*, **106**, 563.
- Fesen, R.A., Blair, W.P., Kirshner, R.P.: 1985, *Astrophys. J.*, **292**, 29.
- Filipović, M.D., Haberl, F., Winkler, P.F., Pietsch, W., Payne, J.L., Crawford, E.J., de Horta, A.Y., Stootman, F.H., Reaser, B.E.: 2008, *Astron. Astrophys.*, **485**, 63.
- Filipović, M.D., Payne, J.L., Reid, W., Danforth, C.W., Staveley-Smith, L., Jones, P.A., White, G.L.: 2005, *Mon. Not. R. Astron. Soc.*, **364**, 217.
- Freedman, W.L., Madore, B.F., Hawley, S.L., Horowitz, I.K., Mould, J., Navarrete, M., Sallmen, S.: 1992, *Astrophys. J.*, **396**, 80.
- Freedman, W.L., Madore, B.F., Gibson, B.K., Ferrarese, L., Kelson, D.D., Sakai, S., Mould, J.R., Kennicutt, R.C. Jr., Ford, H.C., Graham, J.A., Huchra, J.P., Hughes, S.M.G., Illingworth, G.D., Macri, L.M., Stetson, P.B.: 2001, *Astrophys. J.*, **553**, 47.
- Ganda, K., Falcón-Barroso, J., Peletier, R.F., Cappellari, M., Emsellem, E., McDermid, R.M., de Zeeuw, P.T., Carollo, C.M.: 2006, *Mon. Not. R. Astron. Soc.*, **367**, 46.
- Ghosh, K.K., Saripalli, L., Gandhi, P., Foellmi, C.,

- Gutiérrez, C.M., López-Corredoira, M.: 2009, *Astron. J.*, **137**, 3263.
- Gieren, W., Pietrzyński, G., Walker, A., Bresolin, F., Minniti, D., Kudritzki, R., Udalski, A., Soszyński, I., Fouqué, P., Storm, J., Bono, G.: 2004, *Astron. J.*, **128**, 1167.
- Gieren, W., Pietrzyński, G., Soszyński, I., Bresolin, F., Kudritzki, R.P., Minniti, D., Storm, J.: 2005, *Astrophys. J.*, **628**, 695.
- Gil de Paz, A., Boissier, S., Madore, B.F., Seibert, M., Joe, Y.H., Boselli, A., Wyder, T.K., Thilker, D., Bianchi, L., Rey, S., Rich, R.M., Barlow, T.A., Conrow, T., Forster, K., Friedman, P.G., Martin, D.C., Morrissey, P., Neff, S.G., Schiminovich, D., Small, T., Donas, J., Heckman, T.M., Lee, Y., Milliard, B., Szalay, A.S., Yi, S.: 2007, *Astrophys. J. Suppl. Ser.*, **173**, 185.
- Girardi, L., Dalcanton, J., Williams, B., de Jong, R., Gallart, C., Monelli, M., Groenewegen, M.A.T., Holtzman, J.A., Olsen, K.A.G., Seth, A.C., Weisz, D.R., the ANGST/ANGRRR Collaboration: 2008, *Publ. Astron. Soc. Pac.*, **120**, 583.
- Giozzi, M., Satyapal, S., Eracleous, M., Titarchuk, L., Cheung, C.C.: 2009, *Astrophys. J.*, **700**, 1759.
- Gogarten, S.M., Dalcanton, J.J., Williams, B.F., Seth, A.C., Dolphin, A., Weisz, D., Skillman, E., Holtzman, J., Cole, A., Girardi, L., de Jong, R.S., Karachentsev, I.D., Olsen, K., Rosema, K.: 2009a, *Astrophys. J.*, **691**, 115.
- Gogarten, S.M., Dalcanton, J.J., Murphy, J.W., Williams, B.F., Gilbert, K., Dolphin, A.: 2009b, *Astrophys. J.*, **703**, 300.
- Gogarten, S.M., Dalcanton, J.J., Williams, B.F., Roškar, R., Holtzman, J., Seth, A.C., Dolphin, A., Weisz, D., Cole, A., Debattista, V.P., Gilbert, K.M., Olsen, K., Skillman, E., de Jong, R.S., Karachentsev, I.D., Quinn, T.R.: 2010, *Astrophys. J.*, **712**, 858.
- González Delgado, R.M., Pérez, E., Cid Fernandes, R., Schmitt, H.: 2008, *Astron. J.*, **135**, 747.
- Graham, A.W., Erwin, P., Caon, N., Trujillo, I.: 2001, *Astrophys. J. Lett.*, **563**, 11.
- Guerrero, M.A., Chu, Y.: 2008, *Astrophys. J. Suppl. Ser.*, **177**, 216.
- Holwerda, B.W., Keel, W.C., Williams, B., Dalcanton, J.J., de Jong, R.S.: 2009, *Astron. J.*, **137**, 3000.
- Hoopes, C.G., Walterbos, R.A.M., Greenwalt, B.E.: 1996, *Astron. J.*, **112**, 1429.
- Karachentsev, I.D., Grebel, E.K., Sharina, M.E., Dolphin, A.E., Geisler, D., Guhathakurta, P., Hodge, P.W., Karachentseva, V.E., Sarajedini, A., Seitzer, P.: 2003, *Astron. Astrophys.*, **404**, 93.
- Kim, S.C., Sung, H., Park, H.S., Sung, E.C.: 2004, *Chinese J. Astron. Astrophys.*, **4**, 299.
- Kornei, K.A., McCrady, N.: 2009, *Astrophys. J.*, **697**, 1180.
- Kudritzki, R., Urbaneja, M.A., Bresolin, F., Przybilla, N., Gieren, W., Pietrzyński, G.: 2008, *Astrophys. J.*, **681**, 269.
- Kuntz, K.D., Snowden, S.L.: 2010, *Astrophys. J. Suppl. Ser.*, **188**, 46.
- Larsen, S.S.: 2004, *Astron. Astrophys.*, **416**, 537.
- Lauer, T.R., Faber, S.M., Gebhardt, K., Richstone, D., Tremaine, S., Ajhar, E.A., Aller, M.C., Bender, R., Dressler, A., Filippenko, A.V., Green, R., Grillmair, C.J., Ho, L.C., Kormendy, J., Magorrian, J., Pinkney, J., Siopis, C.: 2005, *Astron. J.*, **129**, 2138.
- Lauer, T.R., Gebhardt, K., Faber, S.M., Richstone, D., Tremaine, S., Kormendy, J., Aller, M.C., Bender, R., Dressler, A., Filippenko, A.V., Green, R., Ho, L.C.: 2007a, *Astrophys. J.*, **664**, 226.
- Lauer, T.R., Faber, S.M., Richstone, D., Gebhardt, K., Tremaine, S., Postman, M., Dressler, A., Aller, M.C., Filippenko, A.V., Green, R., Ho, L.C., Kormendy, J., Magorrian, J., Pinkney, J.: 2007b, *Astrophys. J.*, **662**, 808.
- Lianou, S., Grebel, E.K., Koch, A.: 2009, *Astronomische Nachrichten*, **330**, 995.
- Long, K.S.: 1996, in McCray, R., Wang, Z., eds, *IAU Colloq. 145: Supernovae and Supernova Remnants*, Cambridge University Press, 1996, 349.
- Mathewson, D.S., Clarke, J.N.: 1972, *Astrophys. J. Lett.*, **178**, 105.
- Mathewson, D.S., Clarke, J.N.: 1973a, *Astrophys. J.*, **179**, 89.
- Mathewson, D.S., Clarke, J.N.: 1973b, *Astrophys. J.*, **180**, 725.
- Mathewson, D.S., Clarke, J.N.: 1973c, *Astrophys. J.*, **182**, 697.
- Matonick, D.M., Fesen, R.A.: 1997, *Astrophys. J. Suppl. Ser.*, **112**, 49.
- Maund, J.R., Smartt, S.J.: 2009, *Science*, **324**, 486.
- Melbourne, J., Williams, B., Dalcanton, J., Ammons, S.M., Max, C., Koo, D.C., Girardi, L., Dolphin, A.: 2010, *Astrophys. J.*, **712**, 469.
- Mickaelian, A.M.: 2004, *Astron. Astrophys.*, **426**, 367.
- Millar, W.C., White, G.L., Filipović, M.D., Payne, J.L., Crawford, E.J., Pannuti, T.G., Staggs, W.D.: 2011, *Astron. Astrophys. Suppl. Ser.*, **332**, 221.
- Milone, A.P., Villanova, S., Bedin, L.R., Piotto, G., Carraro, G., Anderson, J., King, I.R., Zaggia,

- S.: 2006, *Astron. Astrophys.*, **456**, 517
- Montes, G., Pérez-Torres, M.A., Alberdi, A., González, R.F.: 2009, *Astrophys. J.*, **705**, 899.
- Mould, J., Sakai, S.: 2008, *Astrophys. J. Lett.*, **686**, 75.
- Nantais, J.B., Huchra, J.P., Barmby, P., Olsen, K.A.G.: 2010, *Astron. J.*, **139**, 1178.
- Pannuti, T.G., Duric, N., Lacey, C.K., Goss, W.M., Hoopes, C.G., Walterbos, R.A.M., Magnor, M.A.: 2000, *Astrophys. J.*, **544**, 780.
- Pannuti, T.G., Schlegel, E.M., Lacey, C.K.: 2007, *Astron. J.*, **133**, 1361.
- Payne, J.L., Filipović, M.D., Pannuti, T.G., Jones, P.A., Duric, N., White, G.L., Carpano, S.: 2004, *Astron. Astrophys.*, **425**, 443.
- Payne, J.L., White, G.L., Filipović, M.D.: 2008, *Mon. Not. R. Astron. Soc.*, **383**, 1175.
- Peeples, M.S., Martini, P.: 2006, *Astrophys. J.*, **652**, 1097.
- Pietrzyński, G., Gieren, W., Fouqué, P., Pont, F.: 2001, *Astron. Astrophys.*, **371**, 497.
- Puche, D., Carignan, C., Bosma, A.: 1990, *Astron. J.*, **100**, 1468.
- Read, A.M., Pietsch, W.: 2001, *Astron. Astrophys.*, **373**, 473.
- Read, A.M., Ponman, T.J., Strickland, D.K.: 1997, *Mon. Not. R. Astron. Soc.*, **286**, 626.
- Richstone, D.: 2000, Hubble Space Telescope Proposal 8591.
- Rizzi, L., Bresolin, F., Kudritzki, R., Gieren, W., Pietrzyński, G.: 2006, *Astrophys. J.*, **638**, 766.
- Rizzi, L., Tully, R.B., Makarov, D., Makarova, L., Dolphin, A.E., Sakai, S., Shaya, E.J.: 2007, *Astrophys. J.*, **661**, 815.
- Rosolowsky, E., Blitz, L.: 2005, *Astrophys. J.*, **623**, 826.
- Rossa, J., van der Marel, R.P., Böker, T., Gerssen, J., Ho, L.C., Rix, H., Shields, J.C., Walcher, C.: 2006, *Astron. J.*, **132**, 1074.
- Schild, H., Crowther, P.A., Abbott, J.B., Schmutz, W.: 2003, *Astron. Astrophys.*, **397**, 859.
- Schinnerer, E., Böker, T., Meier, D.S.: 2003, *Astrophys. J. Lett.*, **591**, 115.
- Schinnerer, E., Böker, T., Emsellem, E., Lisenfeld, U.: 2006, *Astrophys. J.*, **649**, 181.
- Seth, A., Agüeros, M., Lee, D., Basu-Zych, A.: 2008, *Astrophys. J.*, **678**, 116.
- Shaw, R.A., Reid, W.A., Parker, Q.A.: 2007, *Publ. Astron. Soc. Pac.*, **119**, 19.
- Shaw, R.A., Stanghellini, L., Villaver, E., Mutchler, M.: 2006, *Astrophys. J. Suppl. Ser.*, **167**, 201.
- Siopis, C., Gebhardt, K., Lauer, T.R., Kormendy, J., Pinkney, J., Richstone, D., Faber, S.M., Tremaine, S., Aller, M.C., Bender, R., Bower, G., Dressler, A., Filippenko, A.V., Green, R., Ho, L.C., Magorrian, J.: 2009, *Astrophys. J.*, **693**, 946.
- Smartt, S.J., Maund, J.R., Hendry, M.A., Tout, C.A., Gilmore, G.F., Mattila, S., Benn, C.R.: 2004, *Science*, **303**, 499.
- Soffner, T., Mendez, R.H., Jacoby, G.H., Ciardullo, R., Roth, M.M., Kudritzki, R.P.: 1996, *Astron. Astrophys.*, **306**, 9.
- Strom, R.C.: 1996, in McCray, R., Wang, Z., eds, *IAU Colloq. 145: Supernovae and Supernova Remnants*, Cambridge University Press, 1996, 333.
- Sugerman, B.E.K.: 2005, *Astrophys. J. Lett.*, **632**, 17.
- Sugerman, B.E.K., Ercolano, B., Barlow, M.J., Tielens, A.G.G.M., Clayton, G.C., Zijlstra, A.A., Meixner, M., Speck, A., Gledhill, T.M., Panagia, N., Cohen, M., Gordon, K.D., Meyer, M., Fabbri, J., Bowey, J.E., Welch, D.L., Regan, M.W., Kennicutt, R.C.: 2006, *Science*, **313**, 196.
- Tikhonov, N.A., Galazutdinova, O.A.: 2005a, *Astrophysics*, **48**, 221.
- Tikhonov, N.A., Galazutdinova, O.A.: 2009, *Astronomy Letters*, **35**, 748.
- Tikhonov, N.A., Galazutdinova, O.A., Drozdovsky, I.O.: 2005b, *Astron. Astrophys.*, **431**, 127.
- Tully, R.B., Fisher, J.R.: 1988, *Catalog of Nearby Galaxies*, Cambridge University Press, 1988.
- Tully, R.B., Rizzi, L., Dolphin, A.E., Karachentsev, I.D., Karachentseva, V.E., Makarov, D.I., Makarova, L., Sakai, S., Shaya, E.J.: 2006, *Astron. J.*, **132**, 729.
- Urošević, D., Pannuti, T.G., Duric, N., Theodorou, A.: 2005, *Astron. Astrophys.*, **435**, 437.
- Van Dyk, S.D., Li, W., Filippenko, A.V.: 2003, *Publ. Astron. Soc. Pac.*, **115**, 1289.
- Wadadekar, Y., Casertano, S., Hook, R., Kızıltan, B., Koekemoer, A., Ferguson, H., Denchev, D.: 2006, *Publ. Astron. Soc. Pac.*, **118**, 450.
- Walcher, C.J., van der Marel, R.P., McLaughlin, D., Rix, H., Böker, T., Häring, N., Ho, L.C., Sarzi, M., Shields, J.C.: 2005, *Astrophys. J.*, **618**, 237.
- Williams, B.F., Dalcanton, J.J., Seth, A.C., Weisz, D., Dolphin, A., Skillman, E., Harris, J., Holtzman, J., Girardi, L., de Jong, R.S., Olsen, K., Cole, A., Gallart, C., Gogarten, S.M., Hidalgo, S.L., Mateo, M., Rosema, K., Stetson, P.B., Quinn, T.: 2009, *Astron. J.*, **137**, 419.
- Williams, B.F., Dalcanton, J.J., Dolphin, A.E., Holtzman, J., Sarajedini, A.: 2009, *Astro-*

phys. J. Lett., **695**, 15.

Williams, B.F., Dalcanton, J.J., Stilp, A., Gilbert, K.M., Roškar, R., Seth, A.C., Weisz, D., Dolphin, A., Gogarten, S.M., Skillman, E., Holtzman, J.: 2010, *Astrophys. J.*, **709**, 135.

Windhorst, R.A., Taylor, V.A., Jansen, R.A., Odewahn, S.C., Chiarenza, C.A.T., Conselice, C.J., de Grijs, R., de Jong, R.S., Mackenty, J.W., Eskridge, P.B., Frogel, J.A., Gallagher, J.S. III, Hibbard, J.E., Matthews, L.D., O'Connell, R.W.: 2002, *Astrophys. J. Suppl. Ser.*, **143**, 113.

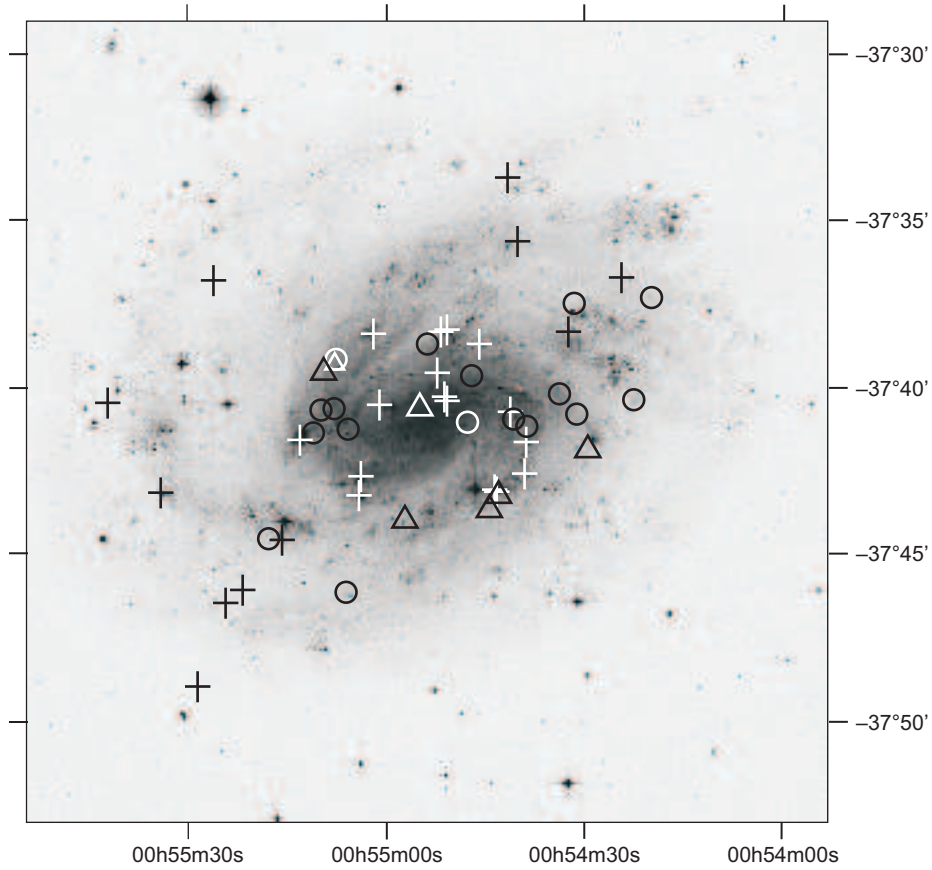


Figure 1. A DSS image of NGC 300 with the positions (in J2000.0 coordinates) indicated of the 51 SNRs and candidate SNRs considered by the present study. Radio sources (SNRs and SNR candidates only) from P04 are shown with crosses. Optical candidates with line ratios measured with long-slit spectra (from BL97) are shown as circles and optical candidates with line ratios measured by interference filters (BL97) are shown with triangles. Symbols are black or white only for increased contrast. (Figure originally published in MWF11. Southern sky DSS image, courtesy of Royal Observatory Edinburgh, Anglo-Australian Observatory, California Institute of Technology.)

F656N (Wheel: 7 Pos: 2)

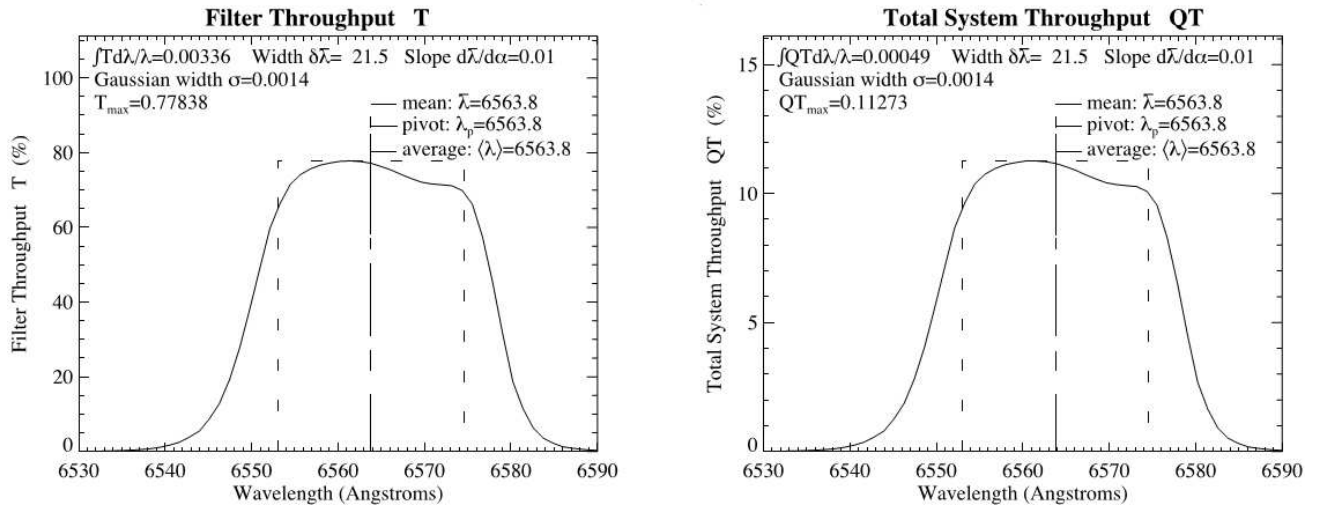


Figure 2. The pass band characteristics of the N565 filter used on the WFPC2 of the HST. (STScI Institute, WFPC2 Observer's Handbook.)

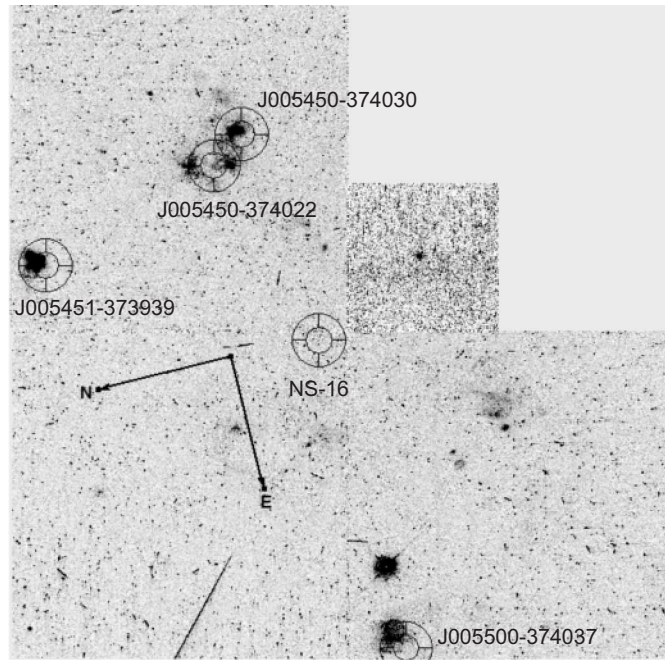


Figure 3. This image is contained in the file `u6713709r_drz.fits` and is here modified using the SAO's DS9 software. The image is a 400 second exposure centered on $\alpha = 00\ 54\ 54.54$, $\delta = -37\ 40\ 35.9$ and rotated $\sim 104^\circ$ east of north. The high-resolution CCD (first quadrant) is centered on the nucleus of NGC 300. The five SNR candidates in this image are described in Table 6. The pandas are centered on each candidate with an inner circle diameter of $6''$ (61.2 pc).

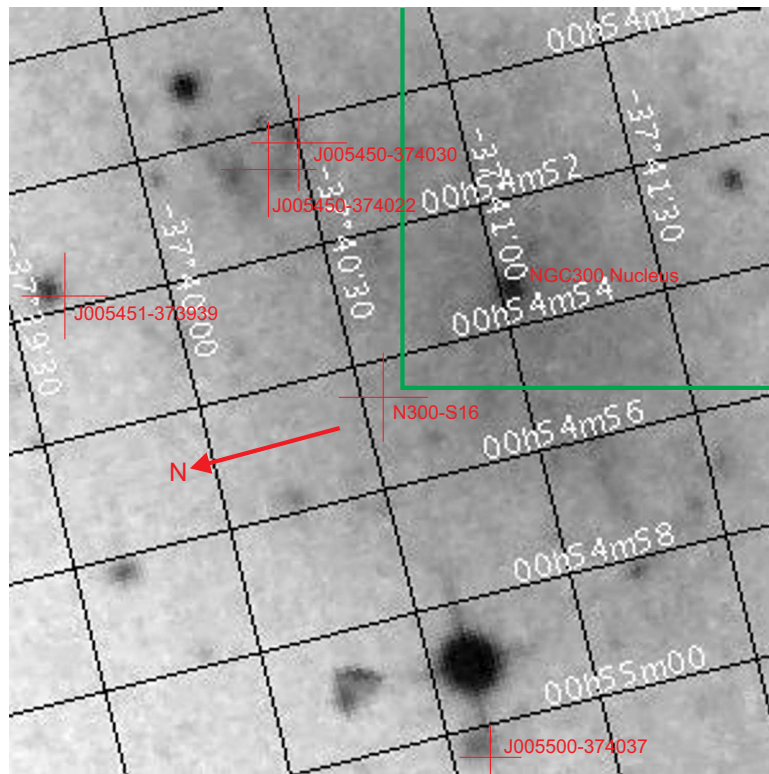


Figure 4. This is the approximate equivalent to the HST image of Fig. 3 created with SkyView using DSS2-Red data. (Southern sky DSS image, Royal Observatory Edinburgh, Anglo-Australian Observatory, California Institute of Technology.)

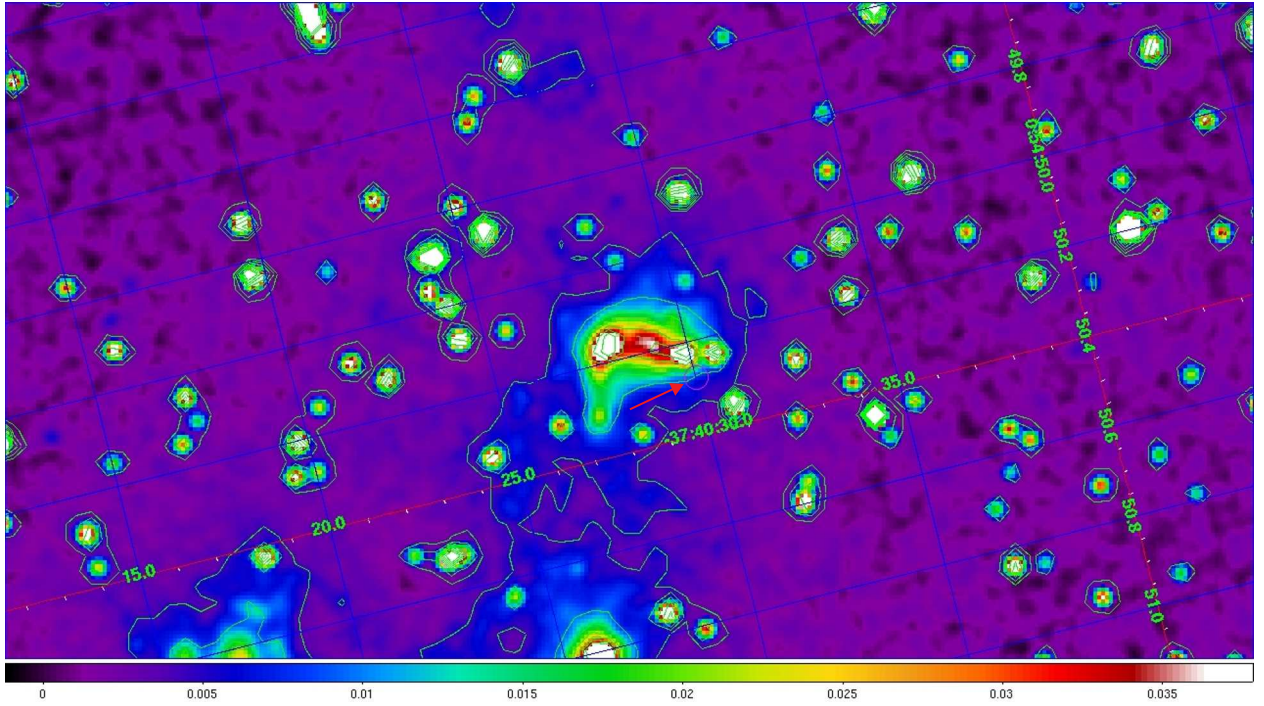


Figure 5. The region surrounding the P04 candidate J005450–374030. The candidate location is shown by the magenta circle (red arrow pointing to it) just to the lower right of center of the intense H II emission. The circle is $1''$ (10.2 pc) in diameter – about twice the 1σ positional error. This false color image and contour plot was created with DS9. Zoom level: 4; Scale: Linear, 98%; Color: SLS; WCS: Equatorial, J2000; Analysis: Contours: 8, Smooth Parameters: 3, Gaussian.

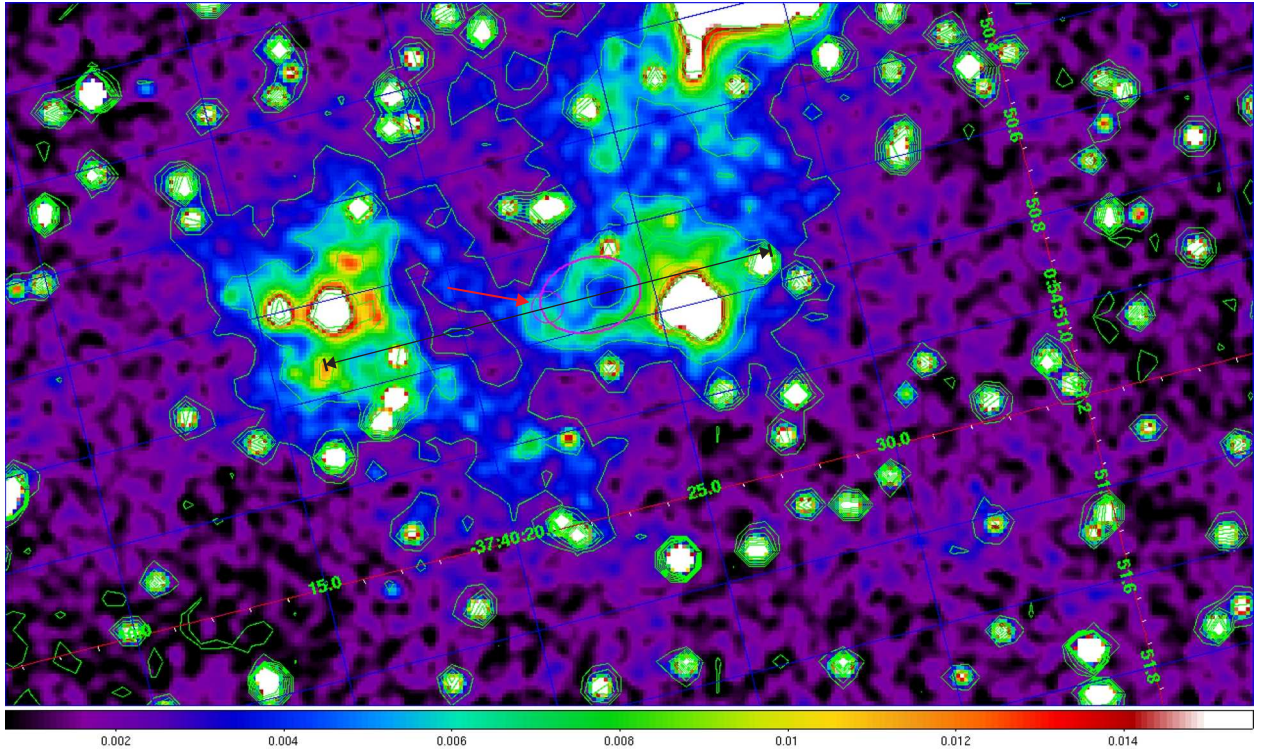


Figure 6. The region surrounding the P04 candidate J005450-374022. The radio source location is shown by the magenta circle (red arrow pointing to it). The circle is $1''$ in diameter ($\sim 2\sigma$ positional error). This false color image and contour plot was created with DS9. Zoom level: 4; Scale: Linear, 98%; Color: SLS; WCS: Equatorial, J2000; Analysis: Contours: 8, Smooth Parameters: 3, Gaussian.

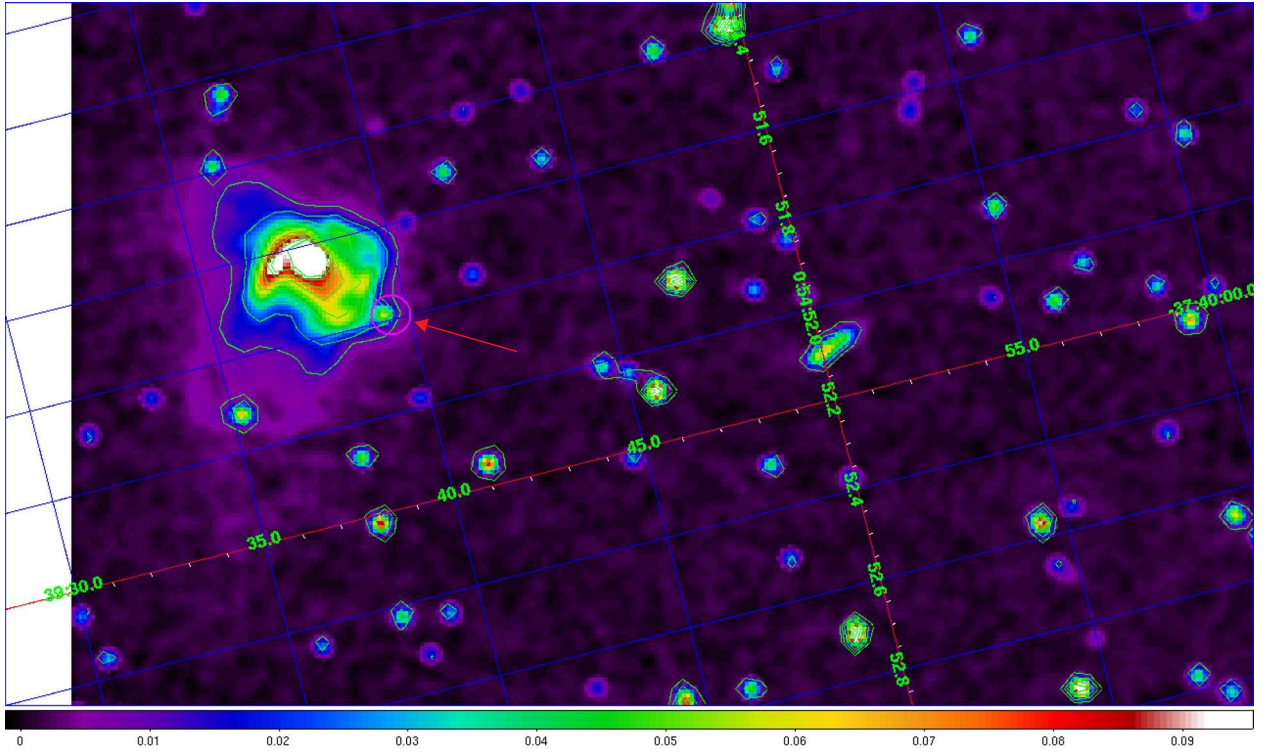


Figure 7. The region surrounding the P04 candidate J005451–373939. The radio source location is shown by the magenta circle (red arrow pointing to it) $1''$ (10.2 pc) in diameter ($\sim 2\sigma$ positional error). This false color image and contour plot was created with DS9. Zoom level: 4; Scale: Linear, 99.5%; Color: SLS; WCS: Equatorial, J2000; Analysis: Contours: 10, Smooth Parameters: 3, Gaussian.

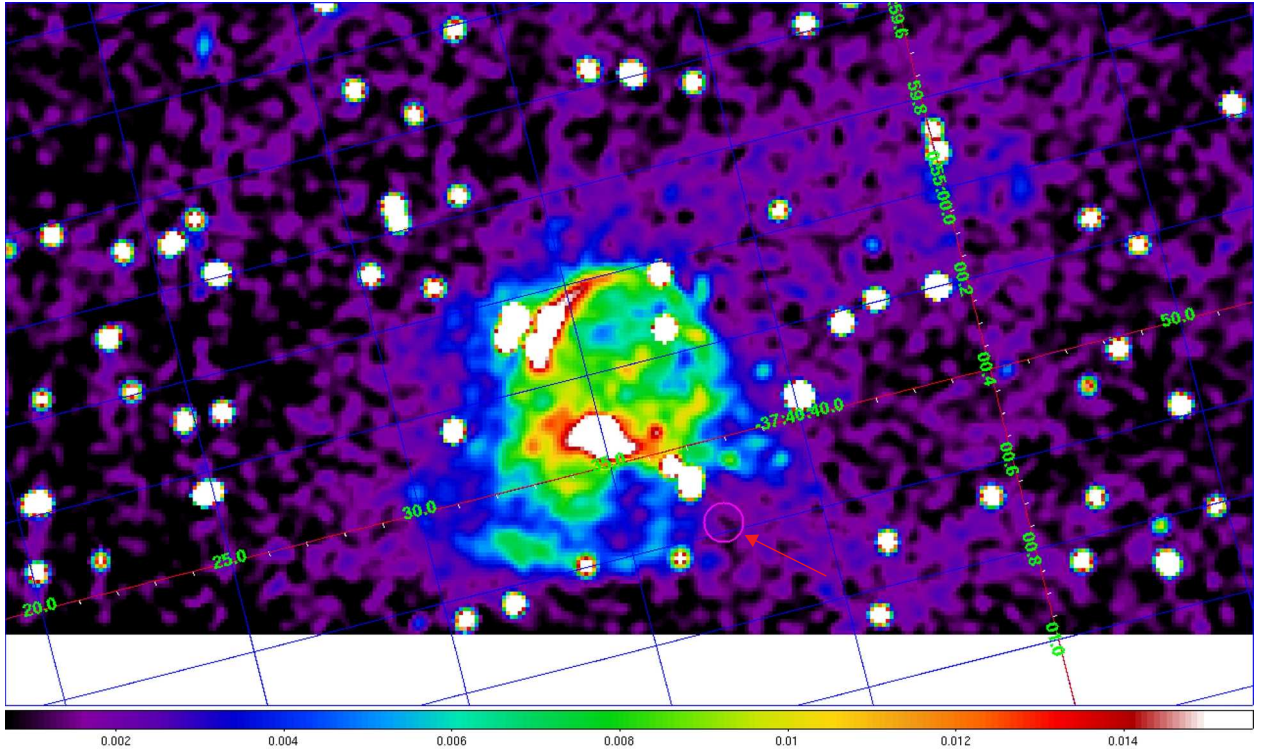


Figure 8. The region surrounding the P04 candidate J005500–374037. The radio source location is shown by the magenta circle (red arrow pointing to it) 1'' in diameter ($\sim 2\sigma$ positional error). This false color image was created with DS9. Zoom level: 4; Scale: Linear, 95%; Color: SLS; WCS: Equatorial, J2000. The contours were not used on this image.

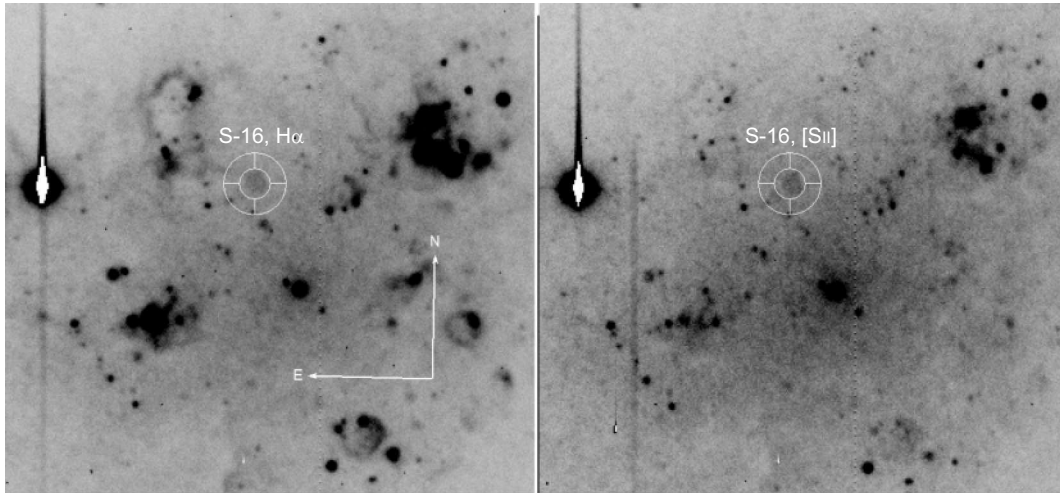


Figure 9. The left image is the $H\alpha$ filter image from BL97. The right image is the $[SII]$ filter image of BL97. An object which could be N300-S16 is visible as a faint smudge in these images. The inner circle of the panda is 8'' (81.6 pc) in diameter.

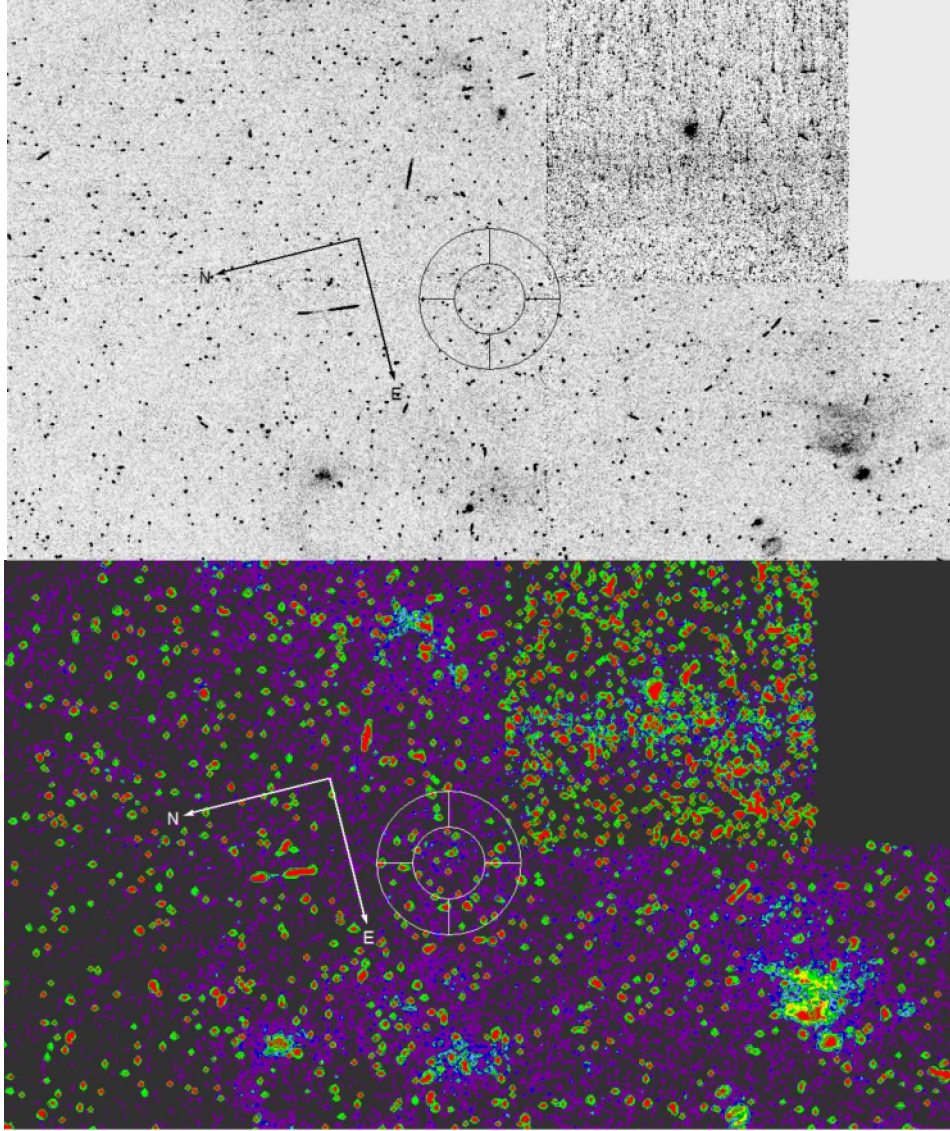


Figure 10. The HST $H\alpha$ image of N300-S16 from shown in inverted gray-scale on top and in AIPS0 with contours on the bottom. In either case no discernible structure is seen in the H gas at the reported location of this candidate SNR. The panda inner circle is $8''$ (81.6 pc) in diameter.

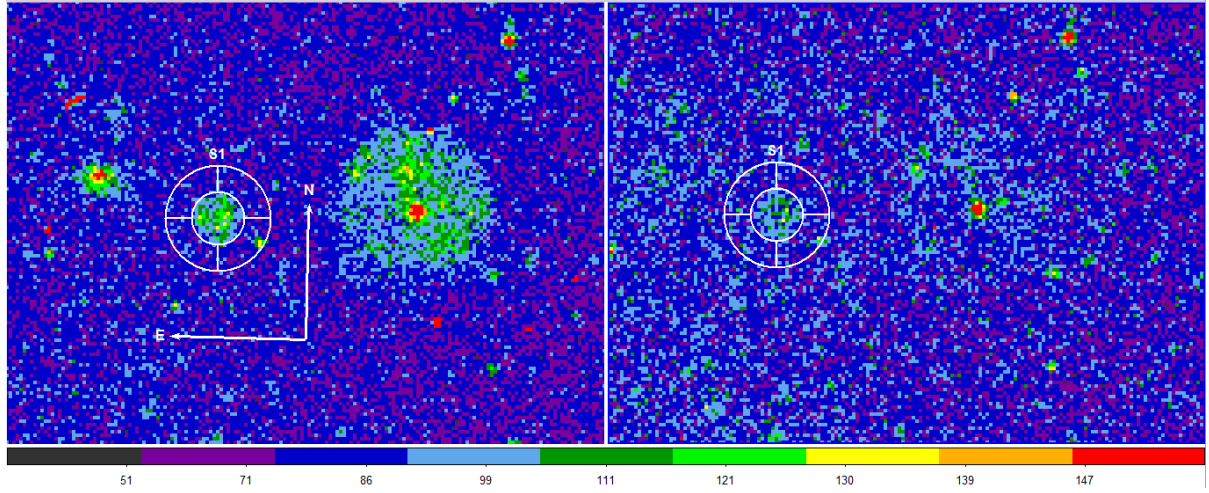


Figure 11. This is the BL97 published location of N300-S1 (α 00 54 19.21, δ -37 37 23.96) as found on the BL97 images (Image D) with 2MASS calibrated astrometry. The $H\alpha$ image is on the left and the $[S II]$ image is on the right. The pandas on both images are centered on the published coordinates for N300-S16, as guided by the 2MASS calibrated WCS for these images. The inner circle of the panda is $5.1''$ (52 pc) and the outer circle is $10.2''$ (104 pc) in diameter. The color scale is AIPS0, Zoom = 4, Scale = ZScale, Squared.

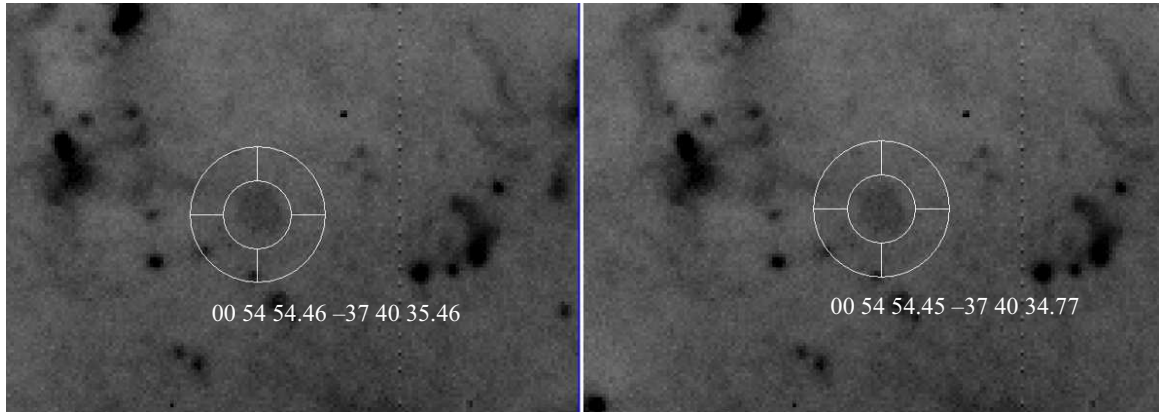


Figure 12. This is the BL97 location of N300-S16. The $H\alpha$ G image is shown on both the left and right with north up and east to the left. The inner circle of the pandas is $4''$. On the left is the reported position of NS16 (BL97) and on the right is the apparent center of the assumed (probable) image of the SNR candidate on the image. The astrometry error is within the typical seeing of two-meter class telescopes and within the reported seeing conditions for the observation.

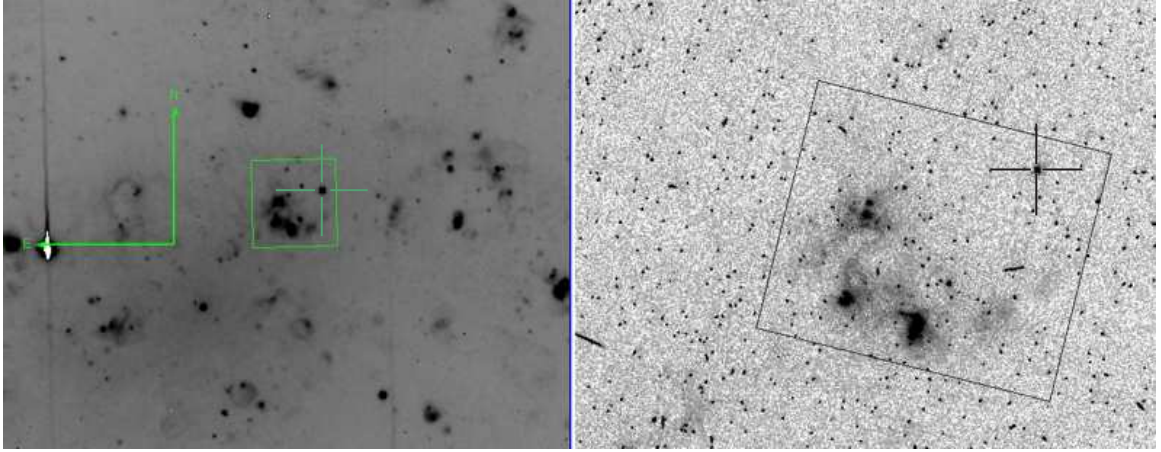


Figure 13. A comparison of the position of a bright star in BL97 G H α image and the HST image u6713709r.drz.fits. The images are both rotated to show north as up, east to the left. The boxes show a set of H II regions used to help identify the star and the selected star is marked with a cross. The measured difference in position is shown in Table 9.

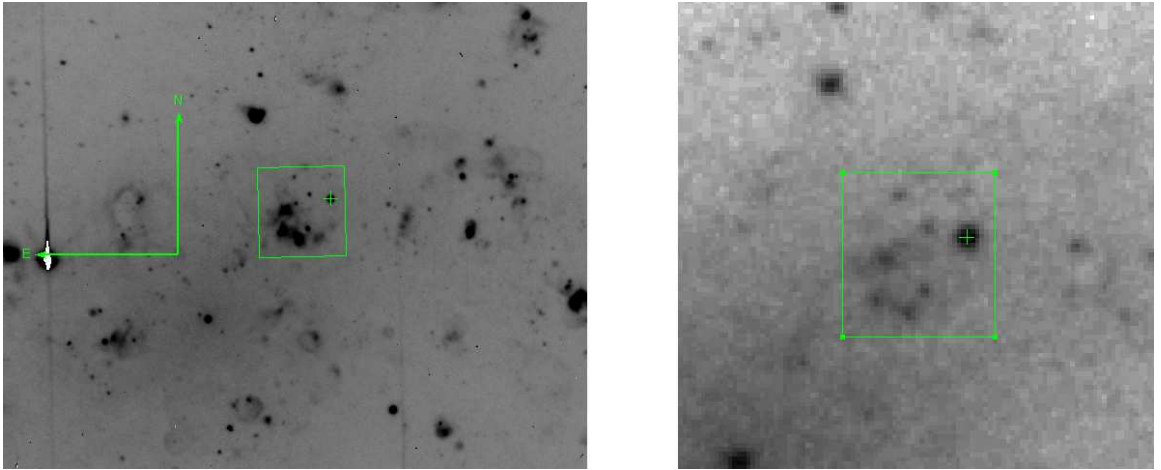


Figure 14. A comparison of the position of a bright star in BL97 G H α image and a DSS2-Red image containing the same H II regions. The image frames are both rotated to show north as up, east to the left. The boxes show a set of H II regions used to help identify the star and the selected star is marked with a small cross. The measured difference in position is shown in Table 9.

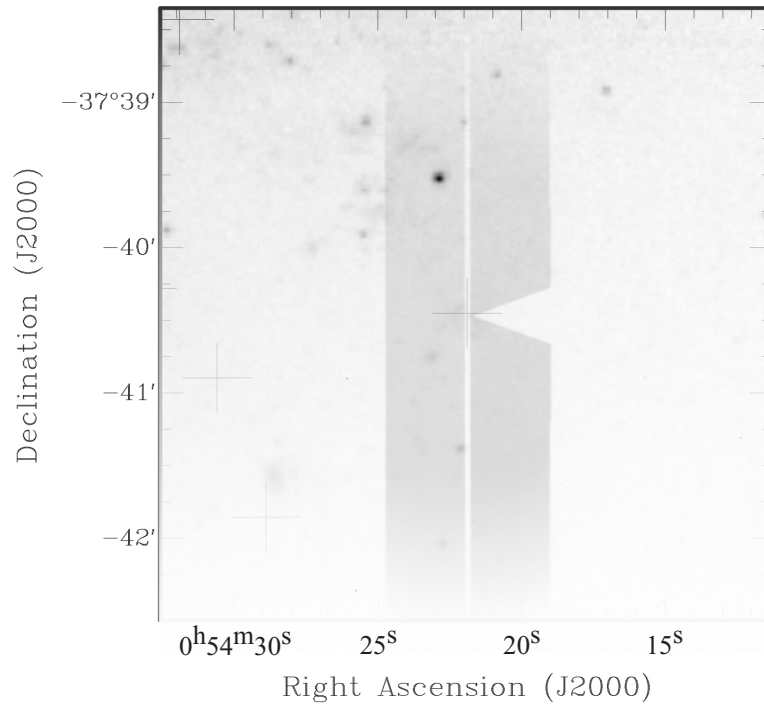


Figure 15. The DBS slit camera image laid on top of the MWF11 finding map for BL97 candidate N300-S2. The circled objects are those which were used for the alignment of the two images. The pointing was exact but there is a significant difference between the measured $[\text{S II}]:\text{H}\alpha$: BL97 = 0.49 and MWF11 = 0.72 ± 0.39 . The large error in flux estimate also allows this object to be below the $[\text{S II}]:\text{H}\alpha$ critical value.

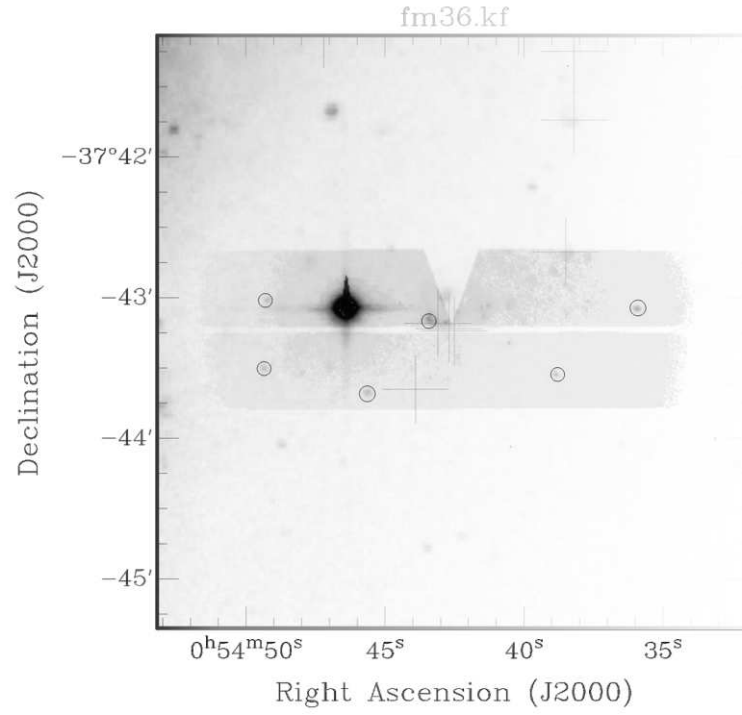


Figure 16. The DBS slit camera image laid on top of the MWF11 finding map for BL97 candidate N300-S11 (lower right cross). The circled objects are those which were used for the alignment of the two images. In this case there is significant source confusion. See text.

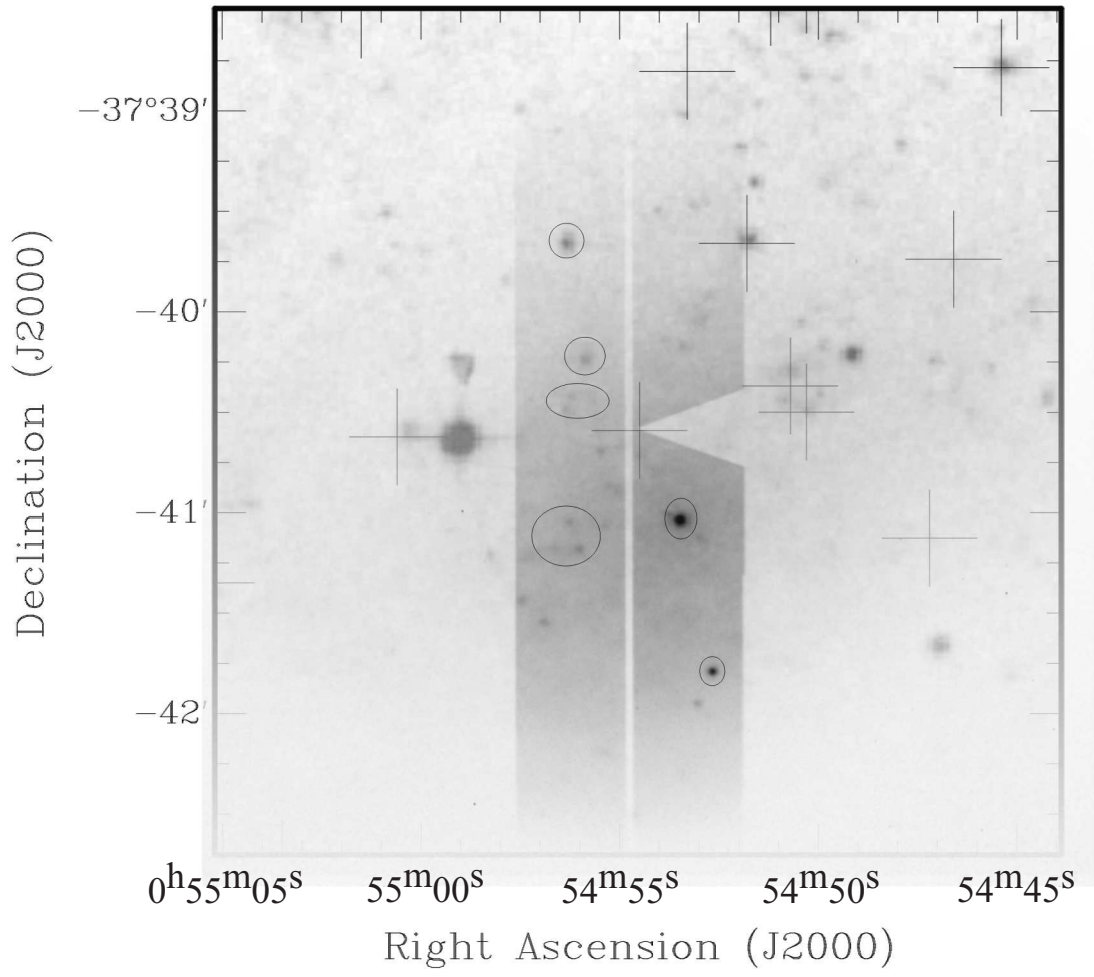


Figure 17. The DBS slit camera image laid on top of the MWF11 finding map for BL97 candidate N300-S16. The circled objects are those which were used for the alignment of the two images. Due to pointing error the slit was not well aligned with the reported position of N300-S16 but a $[\text{S II}]:\text{H}\alpha$ of 0.70 (BL97) or 0.94 ± 0.06 (MWF11) was measured.

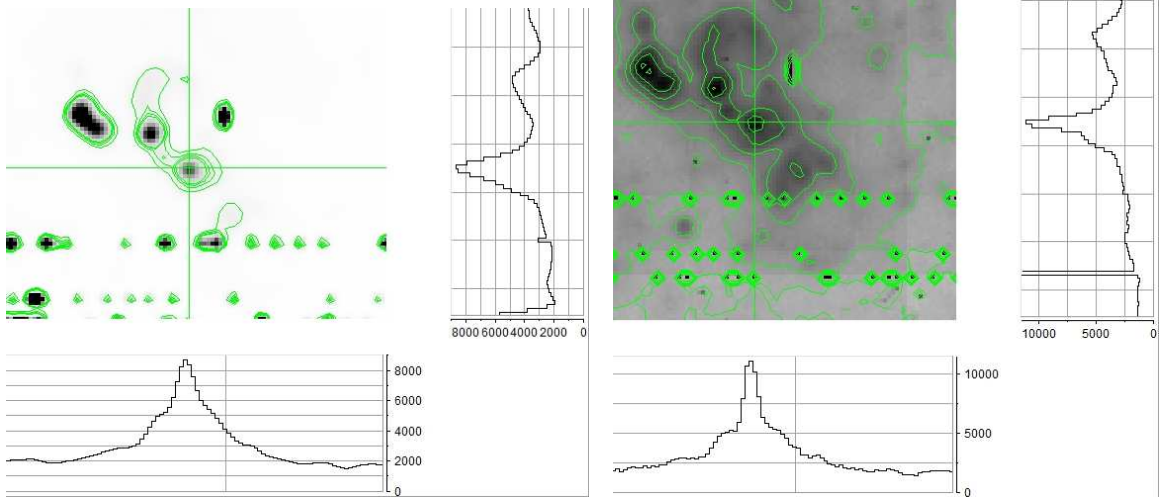


Figure 18. Stacked BL97 H α images of the SNR candidates. The left and right renditions differ in intensity scale, zoom level and contour line count. The profiles of the image stack for x (E-W) and y (N-S) axes are shown below and to the right, respectively. The lines across the rendition (crosshairs) indicate which CCD row (x) and column (y) are displayed in the profiles. These renditions were created with *DS9* after stacking the SNR images with SBIG's *CCDOps* software.

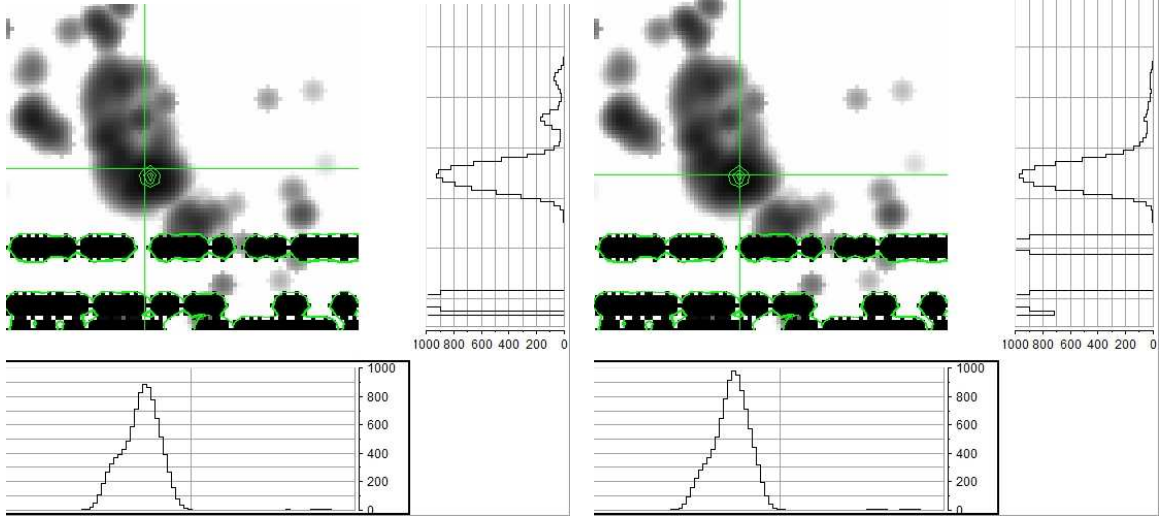


Figure 19. Stacked [S II] images of the BL97 SNR candidates. The left and right renditions differ in the takeoff location of the profiles. The left rendition's profiles are based on the position of the SNR candidate. The right rendition's profiles are based on the pixel with the maximum count. In each rendition, the profiles of the image stack for x (E-W) and y (N-S) axes are shown below and to the right, respectively. The lines (crosshairs) across the rendition indicate which CCD row (x) and column (y) are displayed in the profiles. These rendition were created with *DS9* after stacking the SNR images with SBIG's *CCDOps* software.

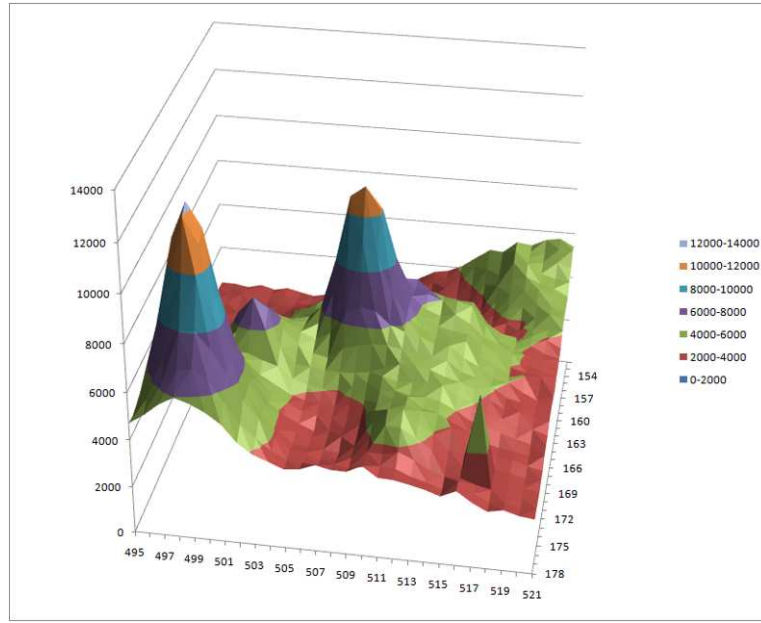


Figure 20. This is a 27×27 pixel (110×110 pc) surface plot the central SNR location of the stacked $H\alpha$ images shown in Fig. 18. The data values of the central 9×9 region is shown in Table 10. A plot of the peak along the x -axis (E-W) at y -axis (N-S) pixel row 165 is shown in Fig. 21.

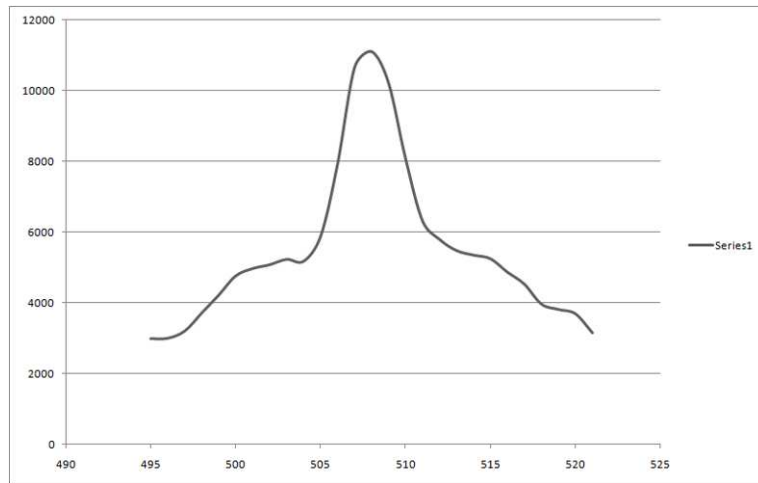


Figure 21. This is a plot of the stacked $H\alpha$ images x -axis (E-W) values in y -axis (N-S) row 165 shown in Fig. 20 and Table 10.

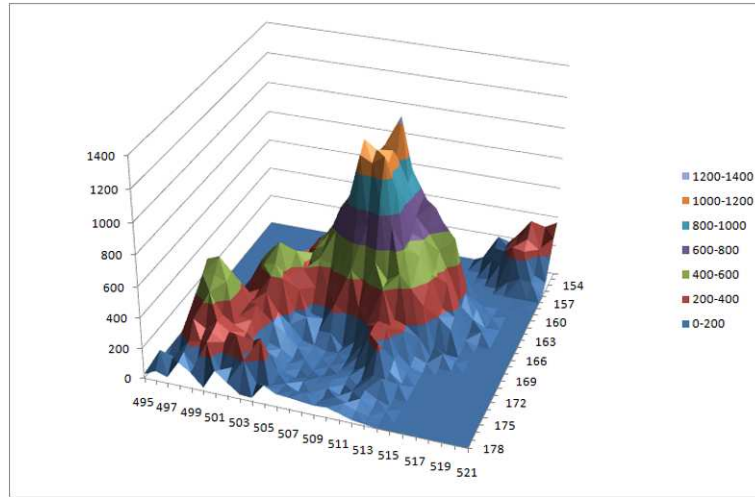


Figure 22. This is a 27×27 pixel (110×110 pc) surface plot the central SNR location of the stacked [S II] images shown in Fig. 19. A plot of the peak along the x -axis (E-W) at y -axis (N-S) pixel row 165 is shown in Fig. 23.

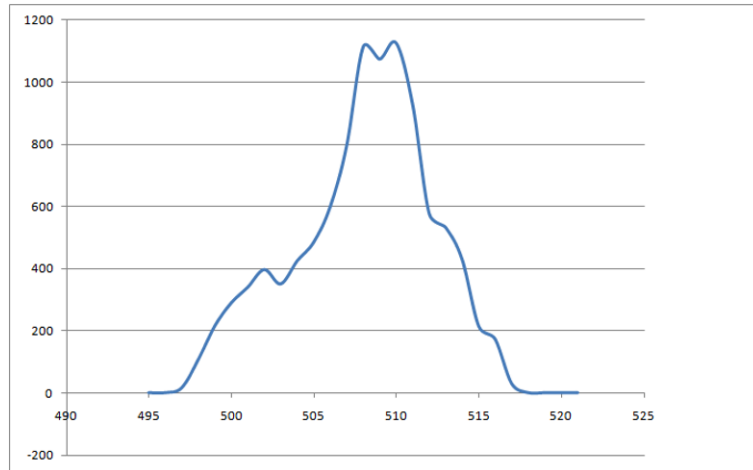


Figure 23. This is a plot of the stacked [S II] images x -axis values in y -axis row 165 shown in Fig. 22. The FWHM is taken at 550 counts as 7 pixels (28 pc).

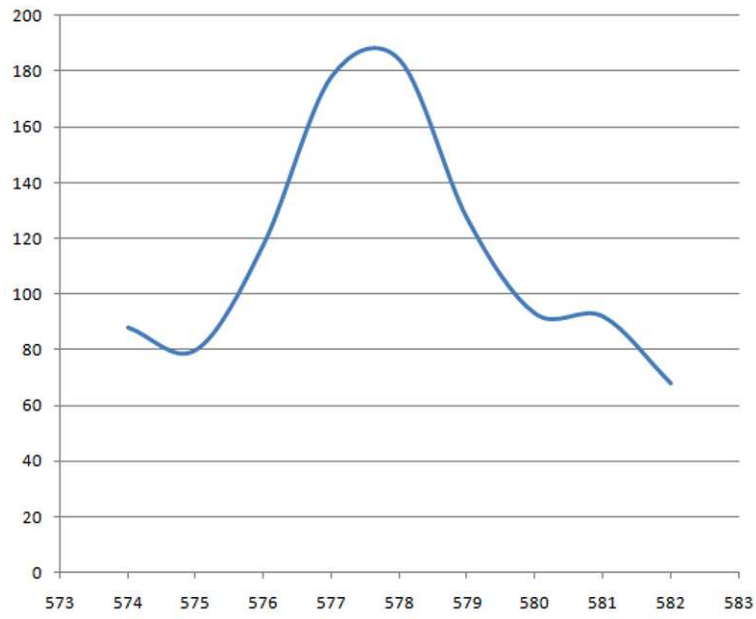


Figure 24. This is the x -axis (E-W) emission profile of a small star from the [S II] J image. The FWHM is taken at 130 count with a pixel width of 3.7 (15 pc).

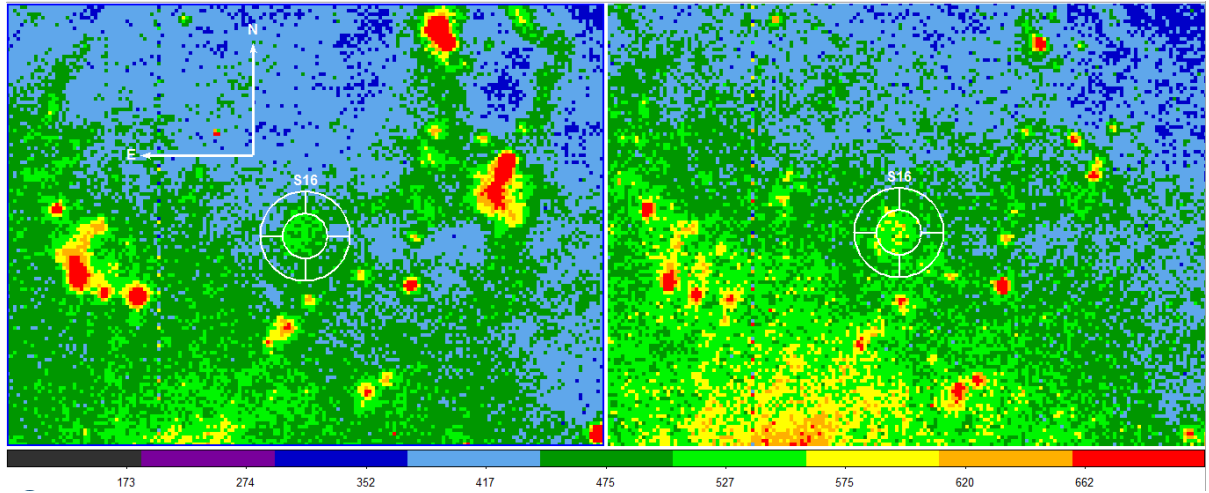


Figure 25. This is the BL97 location of N300-S16 (α 00 54 54.46, δ -37 40 35.46) as found on the BL97 images (G) with 2MASS calibrated astrometry. The $H\alpha$ image is on the left and the [S II] image is on the right. The inner circle of the panda is $5.1''$ (52 pc) in diameter. The color scale is AIPS0, Zoom=4, Scale = ZScale, Squared.

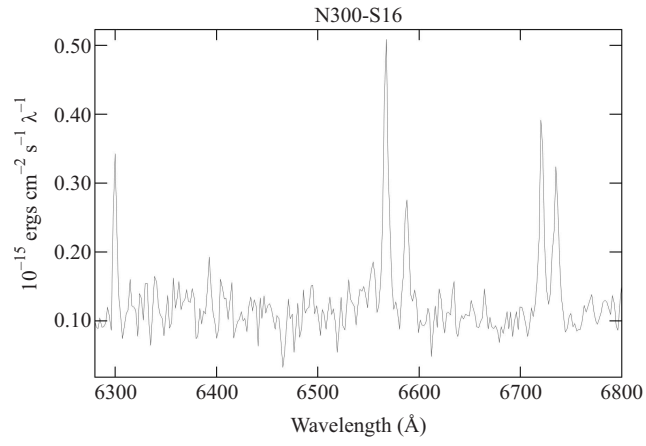


Figure 26. The spectrum of N300-S16 from MWF11. The spectrum also contains a strong [O I] line at 6300 \AA which is an indicator of shock fronts typical of SNRs. Note the broad band noise level in the spectrum and the low flux density.

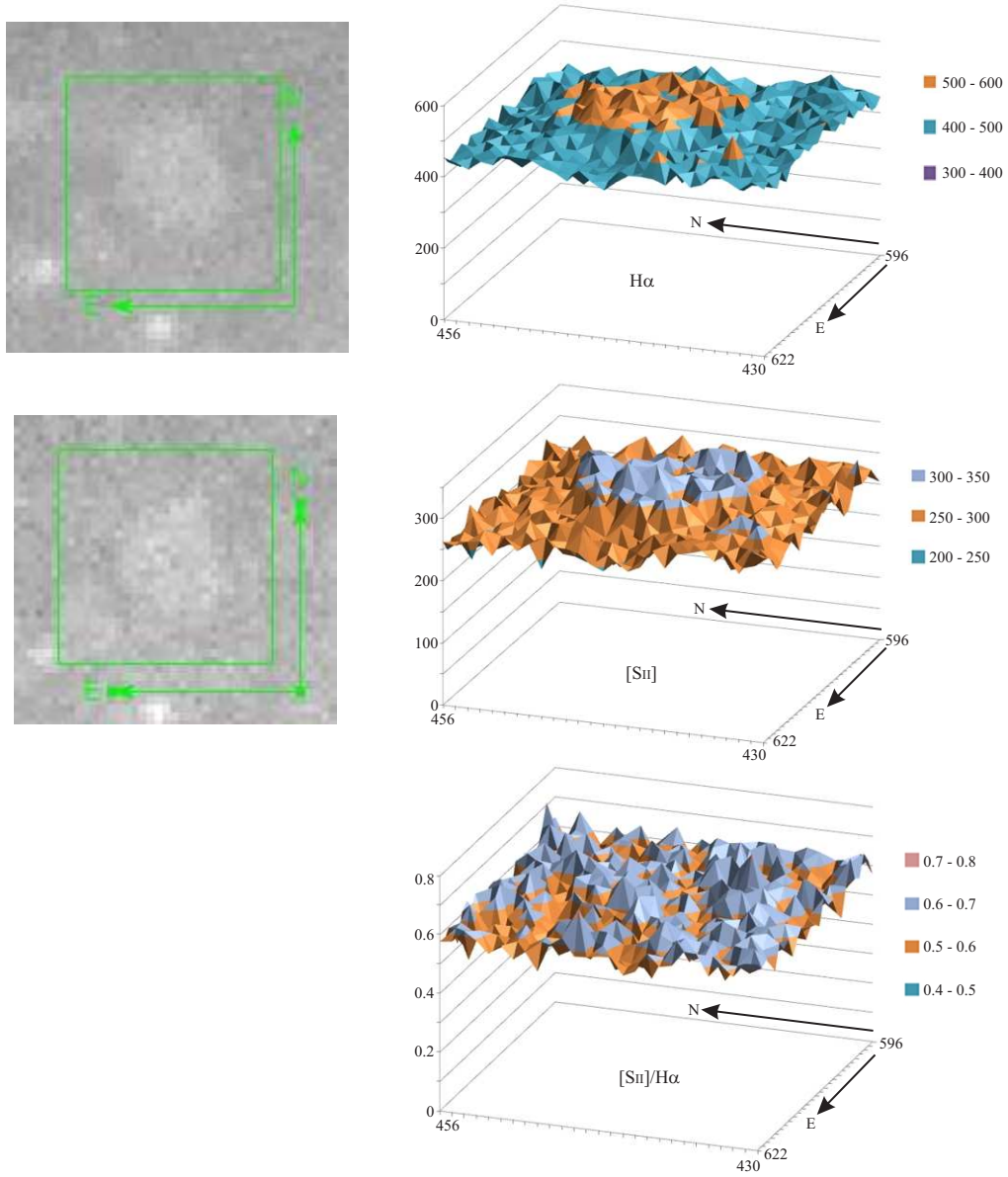


Figure 27. These are 3-D plots of the BL97 image CCD pixel counts of N300-S16 in $H\alpha$ (top) and $[S II]$ (middle). The pixels plotted (a 27×27 array centered on the candidate's coordinates) are shown by the green box in the image tile on the left. The plot is shown on the right. In both cases the emissions are only slightly above the background but clear discernible. The size of the candidate implies it to be at the end of its PDS stage. The 3-D plot on the bottom was the result of dividing the $[S II]$ pixel value by the $H\alpha$ pixel value. The apparent SNR disappears in the high-level noise.

Table 1. Gross Properties of NGC 300 (from MWF11).

Property	Value	Reference
Hubble Type	SA(s)d	Tully et al. (1988) deVaucouleurs et al. (1991)
R.A. (J2000.0)	00 ^h 54 ^m 53.48 ^s	NED
Dec. (J2000.0)	−37°41′03.8″	NED
Galactic Latitude	−77.17°	NED
Radial Velocity	144 km/s (Solar)	Puche et al. (1990) Karachentsev et al. (2003)
Inclination	46°	Tully et al. (1988)
	42.6°	Puche et al. (1990)
Distance	2.1 Mpc	Freedman et al. (1992)
	2.02 Mpc	Freedman et al. (2001)
	1.88 Mpc	Bresolin et al. (2005); Gieren et al. (2005)
Observed Diameter (D_{25})	20.2 arcmin	Tully et al. (1988)
Observed Diameter (UV isophotes)	21.9 x 15.5 arcmin	Gil de Paz et al. (2007)
Galaxy Diameter	22.6 kpc, at 2.1 Mpc	Based on Gil de Paz et al. (2007)
Mass (H I)	$2.4 \times 10^9 M_{\odot}$	Tully et al. (1988)
N_H Column Density	$2.97 \times 10^{20} \text{ cm}^{-2}$	Read et al. (1997)

Note. NED = NASA/IPAC Extragalactic Database (<http://nedwww.ipac.caltech.edu/>).

Table 2. Summary of observational results for the selected objects (from BL97, P04, and MWF11).
The cut-in headers are from MWF11.

1	2	3	4	5	6	7	8
Optical	Radio	RA	Dec	[S II]:H α	[S II]:H α	$\alpha \pm \Delta\alpha$	Diameter
Object	Object	(h m s)	($^{\circ}$ ' ")	(BL97)	(MWF11)	(P04)	(pc, MWF11)
SNRs (MWF11)							
N300-S1		00 54 19.21	-37 37 23.96	0.44	0.46 ± 0.29		38
N300-S2		00 54 21.85	-37 40 27.11	0.49	0.72 ± 0.39		69
N300-S4		00 54 30.62	-37 40 53.75	0.71	0.93 ± 0.04		150
N300-S5		00 54 30.99	-37 37 33.96	0.46	0.56 ± 0.47		
N300-S6	J005431-373825	00 54 31.91	-37 38 25.68	0.60	0.69	- ^a	44
N300-S7		00 54 33.17	-37 40 16.90	0.57	0.57 ± 0.41		31
N300-S8		00 54 38.17	-37 41 14.88	0.61	0.58 ± 0.06		49
N300-S9		00 54 40.20	-37 41 02.12	0.44	0.53 ± 0.23		83
N300-S12		00 54 43.86	-37 43 39.08	0.52	0.73 ± 0.27		22
N300-S13		00 54 46.60	-37 39 44.32	0.59	0.91 ± 0.05		35
N300-S14		00 54 47.15	-37 41 07.63	0.63	1.08 ± 0.24		41
N300-S15		00 54 53.32	-37 38 48.24	0.65	0.57 ± 0.39		12
N300-S16		00 54 54.46	-37 40 35.46	0.70	0.94 ± 0.06		57
N300-S17		00 54 56.68	-37 43 57.70	0.69	0.96 ± 0.15		65
N300-S19		00 55 05.41	-37 41 21.04	0.53	0.70 ± 0.42		30
N300-S20		00 55 05.68	-37 46 13.35	0.75	0.79 ± 0.11		48
N300-S22		00 55 07.50	-37 40 43.20	0.27	0.46 ± 0.38		75
N300-S24		00 55 09.48	-37 40 46.21	0.80	0.64 ± 0.13		100
N300-S25		00 55 10.68	-37 41 27.13	0.64	0.54 ± 0.40		80
N300-S26	J005515-374439	00 55 15.46	-37 44 39.11	0.57	0.86 ± 0.67	-	31
N300-S27		00 55 17.54	-37 44 36.65	0.70	0.64 ± 0.48		66
N300-S28	J005533-374314	00 55 33.76	-37 43 13.13	0.61	0.45 ± 0.15	-	63
Other Objects (H II Regions? MWF11)							
	J005438-374144	00 54 38.16	-37 41 44.2		0.17 ± 0.07	-0.8 ± 0.2	
	J005438-374240	00 54 38.49	-37 42 40.5		0.25 ± 0.02	-	
	J005439-373543	00 54 39.61	-37 35 43.4		0.27	-0.4 ± 0.1	
	J005441-373348	00 54 41.05	-37 33 48.9		0.36	-	
	J005442-374313	00 54 42.70	-37 43 13.3		0.19 ± 0.07	-0.9 ± 0.3	
	J005443-374311	00 54 43.11	-37 43 11.0		0.18 ± 0.09	-0.6 ± 0.2	
	J005445-373847	00 54 45.39	-37 38 47.1		0.11 ± 0.03	-0.3 ± 0.1	
	J005450-374030	00 54 50.28	-37 40 30.0		0.32 ± 0.12	-0.5 ± 0.2	
	J005450-373822	00 54 50.30	-37 38 22.4		0.22 ± 0.14	-0.2 ± 0.2	
	J005450-374022	00 54 50.73	-37 40 22.2		0.38 ± 0.31	-0.3 ± 0.1	130
	J005451-373826	00 54 51.16	-37 38 26.1		0.26 ± 0.16	-1.2 ± 0.7	
	J005451-373939	00 54 51.79	-37 39 39.6		0.10 ± 0.18	-0.1 ± 0.2	
	J005500-374037	00 55 00.58	-37 40 37.4		0.25 ± 0.09	-0.4 ± 0.4	
	J005501-373829	00 55 01.49	-37 38 29.9		0.35 ± 0.12	-0.9 ± 0.1	31
	J005503-374246	00 55 03.50	-37 42 46.0		0.14 ± 0.04	-0.4 ± 0.1	
	J005503-374320	00 55 03.66	-37 43 20.1		0.15 ± 0.08	-0.7 ± 0.3	
	J005512-374140	00 55 12.70	-37 41 40.3		0.08 ± 0.02	-0.7 ± 0.1	
N300-S3		00 54 28.86	-37 41 53.32	0.40	0.24 ± 0.31		26
N300-S10	J005440-374049	00 54 40.87	-37 40 48.73	0.67	0.35 ± 0.15	-0.5 ± 0.3	63
N300-S11		00 54 42.54	-37 43 14.16	0.66	0.30 ± 0.12		150
N300-S18		00 55 01.39	-37 39 18.17	0.53	0.32 ± 0.32		69
N300-S21		00 55 07.15	-37 39 15.17	0.59	0.37 ± 0.30		41
N300-S23		00 55 09.10	-37 39 32.61	0.64	0.31 ± 0.08		43
No Signal (MWF11)							
	J005423-373648	00 54 23.84	-37 36 48.4			-0.7 ± 0.1	
	J005521-374609	00 55 21.35	-37 46 09.6			-1.0 ± 0.3	
	J005523-374632	00 55 23.95	-37 46 32.4			-0.9 ± 0.1	
	J005525-373653	00 55 25.82	-37 36 53.8			-1.0 ± 0.1	
	J005528-374903	00 55 28.25	-37 49 03.3			-0.6 ± 0.3	
	J005541-374033	00 55 41.94	-37 40 33.5			-	

^aSpectral index not determined.

Table 3. Archival HST files organized by filter center wavelength.

1	2	3	4
Wavelength (Å)	Files	Proposal ID	Associated Publications
2993	u8hvp02m.drz	9677	Wadadekar et al. (2006).
4318	j8d702010.drz	9492	Glozzi et al. (2009); Gogarten et al. (2009b);
	j8d702mcq.flt		Nantais et al. (2010); Gogarten et al. (2010);
	j8d702mj.q.flt		Gieren et al. (2004); Bresolin et al. (2005);
	j8d702mrq.flt		Rizzi et al. (2007); Kudritzki et al. (2008);
	j8d703010.drz		Bond et al. (2009); Barth et al. (2009);
	j8d703viq.flt		Dalcanton et al. (2009); Rizzi et al. (2006);
	j8d703vpq.flt		Tikhonov et al. (2005);
	j8d703vxq.flt		Kuntz et al. (2010).
4747	j9ra11010.drz	10915	Berger et al. (2009); Gogarten et al. (2009a);
	j9ra11neq.flt		Holwerda et al. (2009); Lianou et al. (2009);
	j9ra11nfq.flt		Nantais et al. (2010); Williams et al. (2010);
			Melbourne et al. (2010); Gogarten et al. (2010);
			de Mello et al. (2008); Girardi et al. (2008);
			Mould et al. (2008); Bond et al. (2009);
			Williams et al. (2009); Kornei et al. (2009);
			Williams et al. (2009).
5360	j8d702020.drz	9492	See $\lambda = 4318$ Å.
	j8d702mdq.flt		
	j8d702mlq.flt		
	j8d702mtq.flt		
	j8d703020.drz		
	j8d703vj.q.flt		
	j8d703vrq.flt		
	j8d703vzq.flt		
5484	u6713701m.drz	8591	Graham et al. (2001); Schinnerer et al. (2003);
	u6713702r.drz		Larsen (2004); Lauer et al. (2005);
	u6713703r.drz		Rosolowsky et al. (2005); Lauer et al. (2007a);
	u6713704r.drz		Lauer et al. (2007b); González Delgado et al. (2008);
			Dai et al. (2008); Siopis et al. (2009);
			Beifiori et al. (2009).
5741	o6j3bzkyq.flt	9285	Shaw et al. (2006).
5921	j9ra11020.drz	10915	See $\lambda = 4747$ Å.
	j9ra11nhq.flt		
	j9ra11njq.flt		
6001	u8hvp01m.drz	9677	Wadadekar et al. (2006).
6001	u8ixhd01m.drz	9676	Tikhonov et al. (2009); Van Dyk et al. (2003);
	u8ixhd02m.drz		Larsen (2004); Smartt et al. (2004);
			Tikhonov et al. (2005a); Sugerman (2005);
			Milone et al. (2006); Wadadekar et al. (2006);
			Sugerman et al. (2006); Shaw et al. (2007);
			Maund et al. (2009); Guerrero et al. (2008).
6564 (H α)	u6713705r.drz	8591	See $\lambda = 5484$ Å.
	u6713706r.drz		
	u6713707r.drz		
	u6713708r.drz		
	u6713709r.drz		
7996	u65w0201r.drz	8599	Windhorst et al. (2002); Böker et al. (2003a);
	u65w0202r.drz		Larsen (2004); Butler et al. (2004)
	u65w0203r.drz		Walcher et al. (2005); de Grijs et al. (2005);
			Tully et al. (2006); Rossa et al. (2006);
			Schinnerer et al. (2006); Peeples et al. (2006);
			Ganda et al. (2006); Cao et al. (2007);
			Seth et al. (2008); Böker et al. (2003b);
			González Delgado et al. (2008); Ghosh et al. (2009);
			Böker et al. (2004); Andersen et al. (2008);
			Böker et al. (2002).
8057	j9ra11030.drz	10915	See $\lambda = 4747$ Å.
	j9ra11nlq.flt		
	j9ra11nnq.flt		
8060	j8d702030.drz	9492	See $\lambda = 4318$ Å.
	j8d702mfq.flt		
	j8d702moq.flt		
	j8d702mvq.flt		
	j8d702n0q.drz		
	j8d702n0q.flt		
	j8d703030.drz		
	j8d703v1q.flt		
	j8d703vuq.flt		
	j8d703w1q.flt		
	j8d703w6q.drz		
	j8d703w6q.flt		

Table 4. Central Wavelengths of HST Image File Sequences.

1	2	3
Wavelength (Å)	RMS Bandwidth (Å)	Known SNR Ions/Atoms with Wavelengths Å, Fesen et al. 1996
2993	325	Mg I: 2852.13
4318	293	H I: 4340.49 (H γ)
		C II: 4267.00, 4267.26
		[O III]: 4363.21
		[Fe II]: 4177.21, 4243.98,
		4244.81, 4287.40, 4358.10, 4358.37, 4359.34,
		4413.78, 4414.45, 4416.27, 4452.11, 4457.95
		[Fe V]: 4227.20
4747	420	H I: 4861.36 (H β)
		He I: 4713.14, 4713.37, 4921.93
		He II: 4685.68
		[Ne IV]: 4724.17, 4725.60
		Mg I: 4571.10
		[Mg I]: 4562.48
		[Ar IV]: 4711.33, 4740.20
		[Fe II]: 4632.27, 4774.74, 4814.55,
		4889.63, 4889.70, 4905.35
		[Fe III]: 4658.10, 4701.62, 4733.93,
		4754.83, 4769.60, 4777.88, 4813.90, 4881.11,
		4924.50, 4930.50
		[Fe VII]: 4893.40, 4942.50
5360	360	He II: 5411.52
		[N I]: 5197.90, 5200.26
		[Cl III]: 5517.71
		[Ar III]: 5191.82
		[Ca V]: 5309.18
		[Fe II]: 5184.80, 5220.06, 5261.61,
		5268.88, 5273.38, 5296.84, 5333.65, 5376.47,
		5412.64, 5413.34, 5527.33
		[Fe III]: 5270.30
		[Fe VI]: 5277.80, 5335.20, 5424.20, 5426.60, 5484.80
		[Fe XIV]: 5302.86
5484	206	He II: 5411.52
		[O I]: 5577.34
		[Cl III]: 5517.71
		[Fe II]: 5412.64, 5413.34, 5527.33
		[Fe VI]: 5424.20, 5426.60, 5484.80
5741	1836	H I: 4861.36 (H β), 6562.85 (H α)
		He I: 4921.93, 5015.68, (5876)
		He II: 5411.52
		[N I]: 5197.90, 5200.26
		[N II]: 5754.59, 6548.05, 6583.45
		[O I]: 5577.34, 6300.30, 6363.78
		[O III]: 4958.91, 5006.84
		Na I: 5889.95, 5895.92
		[S III]: 6312.06
		[Cl III]: 5517.71
		[Ar III]: 5191.82
		[Ar V]: 6435.10
		[Ca V]: 5309.18
		[Fe II]: 4889.63, 4889.70, 4905.35,
		4973.39, 5039.10, 5043.53, 5072.40, 5107.95,
		5111.63, 5158.00, 5158.81, 5184.80, 5220.06,
		5261.61, 5268.88, 5273.38, 5296.84, 5333.65,
		5376.47, 5412.64, 5413.34, 5527.33
		[Fe III]: 4881.11, 4924.50, 4930.50,
		4985.90, 4987.20, 5270.30
		[Fe VI]: 4972.50, 5145.80, 5176.00,
		5277.80, 5335.20, 5424.20, 5426.60, 5484.80,
		5631.10, 5677.00
		[Fe VII]: 4893.40, 4942.50, 5158.90, 5720.70, 6087.00
		[Fe X]: 6374.51
		[Fe XIV]: 5302.86

^a Unable to find these wavelengths for H I in NIST database.

Continued

Table 4. Central Wavelengths of HST Image File Sequences (continued).

1	2	3
Wavelength (Å)	RMS Bandwidth (Å)	Known SNR Ions/Atoms with Wavelengths Å, Fesen et al. 1996
5921	672	He I: (5876) [N II]: 5754.59 Na I: 5889.95, 5895.92 [Fe VI]: 5631.10, 5677.00 [Fe VII]: 5720.70, 6087.00
6001	638	He I: (5876) [N II]: 5754.59 [O I]: 6300.30 Na I: 5889.95, 5895.92 [S III]: 6312.06 [Fe VII]: 5720.70, 6087.00
6564	54	H I: 6562.85 (H α) [N II]: 6548.05, 6583.45
7996	646	He II: 8236.77 O I: (7774) [Ar III]: 7751.06 [Cr II]: 7999.85, 8125.22, 8229.55, 8308.39 [Fe II]: 7686.19, 7686.90 [Fe XI]: 7891.80 [Ni II]: 8300.99
8057	652	H I: 8345.55, 8359.00, 8374.48 ^a He II: 8236.77 O I: (7774) [Ar III]: 7751.06 [Cr II]: 7999.85, 8125.22, 8229.55, 8308.39, 8357.51 [Fe XI]: 7891.80 [Ni II]: 8300.99
8060	653	H I: 8345.55, 8359.00, 8374.48 ^a He II: 8236.77 O I: (7774) [Ar III]: 7751.06 [Cr II]: 7999.85, 8125.22, 8229.55, 8308.39, 8357.51 [Fe XI]: 7891.80 [Ni II]: 8300.99

^a Unable to find these wavelengths for H I in NIST database.

Table 5. HST filters containing ion/atom species important for SNR identification.

1	2	3
Wavelength (Å)	RMS Bandwidth (Å)	SNR Diagnostic Ions/Atoms with Wavelengths (Å)
5741	1836	H I: 4861.36 (H β), 6562.85 (H α) [N II]: 5754.59, 6548.05, 6583.45 [O I]: 5577.34, 6300.30, 6363.78 [O III]: 4958.91, 5006.84
6001	638	[O I]: 6300.30
6564	54	H I: 6562.85 (H α) [N II]: 6548.05, 6583.45

Table 6. Five candidates found in the H α HST image `u6713709r_drz.fits`. The positions are the J2000 coordinates reported by P04 (radio sources) and BL97 (optical candidates).

1	2	3	4	5	6	7	8
Optical Object	Radio Object	RA (h m s)	Dec ($^{\circ}$ ' ")	[S II]:H α (BL97)	[S II]:H α (MWF11)	$\alpha \pm \Delta\alpha$ (P04)	Diameter (pc, MWF11)
	J005450–374030	00 54 50.28	–37 40 30.0		0.32 ± 0.12	-0.5 ± 0.2	
	J005450–374022	00 54 50.73	–37 40 22.2		0.38 ± 0.31	-0.3 ± 0.1	130
	J005451–373939	00 54 51.79	–37 39 39.6		0.10 ± 0.18	-0.1 ± 0.2	
	J005500–374037	00 55 00.58	–37 40 37.4		0.25 ± 0.09	-0.4 ± 0.4	
N300-S16		00 54 54.46	–37 40 35.46	0.70	0.94 ± 0.06		57

^aSpectral index not determined.**Table 7.** Image center from BL97 and 2MASS calibrated.

1	2	3	4
Image	BL97 Center (h m s $^{\circ}$ ' ")	Calibrated Center (h m s $^{\circ}$ ' ")	Difference (")
D	00 54 23.030 –37 35 50.600	00 54 22.966 –37 35 51.374	1.081
E	00 55 38.770 –37 40 47.900	00 55 38.793 –37 40 48.215	0.420
F	00 55 13.460 –37 40 51.900	00 55 13.550 –37 40 52.086	1.082
G	00 54 47.360 –37 40 50.400	00 54 47.359 –37 40 51.305	0.905
H	00 54 22.840 –37 40 50.700	00 54 22.856 –37 40 52.042	1.356
J	00 55 14.000 –37 45 50.300	00 55 13.987 –37 45 50.463	0.227

Table 8. Calculated pixel positions of BL97 candidate SNRs.

1	2	3	4
Object	BL97 Coordinates (h m s ° ' ")	Image	(x, y) Location (pixel position)
N300-S1	00 54 19.21 -37 37 23.96	D	508, 165
N300-S2	00 54 21.85 -37 40 27.11	H	431, 458
N300-S3	00 54 28.86 -37 41 51.32	H	219, 254
N300-S4	00 54 30.62 -37 40 53.75	H	170, 398
N300-S5	00 54 30.99 -37 37 33.96	D	158, 149
N300-S6	00 54 31.91 -37 38 25.68	D	128, 020
		H	141, 767
N300-S7	00 54 33.17 -37 40 16.90	H	097, 492
N300-S8	00 54 38.17 -37 41 14.88	G	671, 333
N300-S9	00 54 40.20 -37 41 02.12	G	612, 366
N300-S10	00 54 40.87 -37 40 48.73	G	593, 400
N300-S11	00 54 42.54 -37 43 14.16	G	535, 040
N300-S12	00 54 43.86 -37 43 39.08	(I)	
N300-S13	00 54 46.60 -37 39 44.32	G	427, 564
N300-S14	00 54 47.15 -37 41 07.63	G	406, 357
N300-S15	00 54 53.32 -37 38 48.24	G	231, 709
N300-S16	00 54 54.46 -37 40 35.46	G	191, 443
N300-S17	00 54 56.68 -37 43 57.70	(I)	
N300-S18	00 55 01.39 -37 39 18.17	F	762, 629
N300-S19	00 55 05.41 -37 41 21.04	F	636, 323
N300-S20	00 55 05.68 -37 46 13.35	J	645, 336
N300-S21	00 55 07.15 -37 39 15.17	F	592, 639
N300-S22	00 55 07.50 -37 40 43.18	F	577, 419
N300-S23	00 55 09.10 -37 39 32.61	F	535, 597
N300-S24	00 55 09.48 -37 40 46.21	F	518, 413
N300-S25	00 55 10.68 -37 41 27.13	F	482, 311
N300-S26	00 55 15.46 -37 44 39.31	J	361, 579
N300-S27	00 55 17.54 -37 44 36.65	J	299, 587
N300-S28	00 55 33.76 -37 43 13.33	E	541, 034

Table 9. A comparison of positions of a bright star in the image sets. Because the BL97 images were calibrated to 2MASS those star coordinates are used as the standard.

1	2	3	4	5	6
Image Set	RA (J2000)	Δ (")	Dec (J2000)	Δ (")	Distance (")
BL97 (Image G)	00 54 49.146	—	−37 40 11.99	—	—
HST File (u6713709r.drz.fits)	00 54 49.085	−0.061	−37 40 12.13	0.14	0.15
DSS2-Red	00 54 49.099	−0.047	−37 40 12.11	0.12	0.13

Table 10. A 9×9 region of CCD pixel values (37×37 pc) surrounding the central $H\alpha$ peak in Fig. 18. The x -axis (E-W) pixel numbers are across the top and the y -axis (N-S) pixel numbers are along the left side of the table. A surface plot of these data is shown in the central region of Fig. 20 and a line plot of the peak is shown in Fig. 21.

	504	505	506	507	508	509	510	511	512
169	4664	4606	4489	4482	4507	4610	4842	5088	5071
168	5168	4856	4704	5165	5357	5485	5495	5369	5272
167	5400	5122	5478	6374	6677	6588	6046	5802	5665
166	5270	5494	6869	8522	9109	8479	7062	6104	5669
165	5182	5889	7939	10668	11117	10225	8087	6320	5801
164	5088	5611	7712	9893	10624	9952	7889	6366	5851
163	4897	5182	6255	7615	7955	7798	7071	6165	6185
162	4775	4922	5444	5919	6285	6397	6471	6066	6040
161	4709	4740	5362	5681	6046	6129	6120	6164	5652

ОПТИЧКЕ ТЕХНИКЕ ПОСМАТРАЊА ВАН ГАЛАКТИЧКИХ ОСТАТАКА СУПЕРНОВИХ: СЛУЧАЈ НГЦ 300

William C. Millar^{1,2}, Graeme L. White³ and Miroslav D. Filipović^{4,1}

¹*Centre for Astronomy, James Cook University, Townsville, Queensland 4811, Australia*

²*Grand Rapids Community College, 143 Bostwick N.E., Grand Rapids, MI, 49503, USA*
E-mail: wmillar@grcc.edu

³*Charles Sturt University, Locked Bag 588, Wagga Wagga, NSW 2678, Australia*

⁴*University of Western Sydney, Locked Bag 1797, Penrith South DC, NSW 1797, Australia*
E-mail: m.filipovic@uws.edu.au

УДК ...

Оригинални научни рад

У овој студији представљамо посматрачке технике коришћене за спектроскопску идентификацију кандидата остатака супернових у НГЦ 300 из Скулптор Групе галаксија. Главни циљ ове студије односи се на испитивање сврсишодности коришћење параметра $[\text{Si}]:\text{H}\alpha \geq 0.4$ у идентификацији ван-галактичких остатака супернових. Посебна пазња посвећена је чињеници да посматрачки услови као што су видљивост и пози-

циона прецизност телескопа имају доминантну улогу у коришћењу ове технике. Ова студија базира се на архивским посматрањима са Hubble Space Telescope на којима су идентификовани остаци супернових у Скулптор галаксији — НГЦ 300. Наши резултати показују да је применљивост ове технике веома непоуздана и да посматрања у вишој резолуцији су неопходна приликом идентификације ван-галактичких остатака супернових.